Multi-parametric MRI Study of

Brain Insults (*Traumatic Brain Injury and Brain Tumor*) in Animal Models

by

Bharat Annaldas

A Thesis presented in Partial Fulfillment
of the Requirements for the Degree of
Master of Science

Approved July 2014 by the
Graduate Supervisory Committee:

Vikram Kodibagkar, Chair
Sarah Stabenfeldt
Ratan Bhardwaj

ARIZONA STATE UNIVERSITY

August 2014

ABSTRACT

The objective of this small animal pre-clinical research project was to study quantitatively the long-term micro- and macro- structural brain changes employing multi-parametric MRI (Magnetic Resonance Imaging) techniques. Two separate projects make up the basis of this thesis. The first part focuses on obtaining prognostic information at early stages in the case of Traumatic Brain Injury (TBI) in rat animal model using imaging data acquired at 24-hours and 7-days post injury. The obtained parametric T_2 and diffusion values from DTI (Diffusion Tensor Imaging) showed significant deviations in the signal intensities from the control and were potentially useful as an early indicator of the severity of post-traumatic injury damage. DTI was especially critical in distinguishing between the cytotoxic and vasogenic edema and in identification of injury regions resolving to normal control values by day-7. These results indicate the potential of quantitative MRI as a clinical marker in predicting prognosis following TBI. The second part of this thesis focuses on studying the effect of novel therapeutic strategies employing dendritic cell (DC) based vaccinations in mice glioma model. The treatment cohorts included comparing a single dose of Azacytidine drug vs. mice getting three doses of drug per week. Another cohort was used as an untreated control group. The MRI results did not show any significant changes in between the two treated cohorts with no reduction in tumor volumes compared to the control group. The future studies would be focused on issues regarding the optimal dose for the application of DC vaccine. Together, the quantitative MRI plays an important role in the prognosis and diagnosis of the above mentioned pathologies, providing essential information about the anatomical location, micro-structural tissue environment, lesion volume and treatment response.

ACKNOWLEDGEMENTS

Last but not least, I would like to pay high regards to my parents and my kid sister for their unfailing support and continuous encouragement throughout my years of study and through the process of researching and writing this thesis. This accomplishment would not have been possible without them.

Bharat V Annaldas

TABLE OF CONTENTS

LIST OF TABLES

LIST OF FIGURES

ABBREVIATIONS

ADC   =   Apparent Coefficient Diffusion

CT   =   Computed Tomography

CD68   =   Cluster of Differentiation 68
              (a glycoprotein which binds to low density lipoprotein)

DC   =   Dendritic Cells

DTI   =   Diffusion Tensor Imaging

FA   =   Fractional Anisotropy

GFAP   =   Glial Fibrillary Acidic Protein

HBSS   =   Hank's Balanced Salt Solution

MRI   =   Magnetic Resonance Imaging

NMR   =   Nuclear Magnetic Resonance

PBS   =   Phosphate Buffered Saline

ROI   =   Region of interest

TBI   =   Traumatic Brain Injury

1. MAGNETIC RESONANCE IMAGING (MRI)

Magnetic Resonance Imaging or MRI is a medical imaging technique that offers the most sensitive non-invasive way to investigate a sample like human or animal body. It plays an essential role in understanding about the underlying pathology of the disease that can be used to study anatomy, to diagnose a disease or to monitor improvement following a treatment. Compared to the Computer Tomography (CT) and x-ray imaging techniques, MRI provides excellent soft tissue contrast and resolution (the ability to distinguish the differences between two arbitrarily similar but not identical tissues), which makes it very useful in the study of different brain pathologies.

Further in this chapter a brief introduction to the basic principles of MRI followed with quantitative MRI methods used in the present project is provided.

1.1 Basic Principles

Spin is a fundamental property (like electrical charge or mass) of sub-atomic particles such as protons, electrons and neutrons. MRI produces images by exploiting the interaction between the nuclear spins and an externally applied strong homogenous static magnetic field, $\mathbf{B_0}$. When the sample is placed in the magnet, the atomic nuclei or protons with a non-zero spin (ex. hydrogen with a $^1/_2$ spin) present in the body tends to align itself in the direction or against the direction of $\mathbf{B_0}$ almost cancelling each other out. However, a slightly bigger number of protons align in parallel with the applied magnetic field generating a net overall equilibrium magnetization, $\mathbf{M_0}$. In this equilibrium state only longitudinal magnetization ($\mathbf{M_z}$) is present with no transverse magnetization ($\mathbf{M_x}$ or $\mathbf{M_y}$). At this stage RF pulses exactly at the Larmor frequency (the resonance frequency of

protons) are applied to generate a magnetic field $\mathbf{B_1}$ perpendicular to $\mathbf{B_0}$ field. This causes the spins to excite causing them flip to away from the z-axis and gain x- and y-components while precessing (rotating) about the z-axis (Figure 1.2). At this stage the magnetic field $\mathbf{B_0}$ is aligned with the z-axis. The precessing of nuclei in the xy-plane generates a detectable alternating RF field. At the end of the applied RF pulse, the magnetization field $\mathbf{B_1}$ returns to equilibrium from the excited state through interactions with the surrounding environment by a process called relaxation. The relaxation process follows an exponential curve and can be described by two time constants, T_1 and T_2. From a clinical perspective, they are useful because different tissues appear differently in T_1 and T_2 weighted MR scans. For example, T_1 images cause fat to appear bright, fat like the myelin in white matter whereas T_2 weighted images cause water to appear bright like CSF and fat is dark.

1.2 T_1 and T_2 Weighted Images

All molecules have natural motions in the form of vibration, rotation and translation. Smaller molecules like water generally move more rapidly resulting in higher natural frequencies compared to larger molecules like proteins that move more slowly.

T_1 or longitudinal relaxation time **(Figure 1.1 (A))** represents the time required for a substance to regain its longitudinal magnetization (in the z- direction) following an RF pulse. It is usually determined by the thermal interactions between the resonating protons and other protons and other magnetic nuclei in the magnetic environment. These interactions allow the energy absorbed by the protons during resonance to be dispersed to other nuclei. T_2 or transverse relaxation time is a measure of how long the resonating

2

protons remain coherent or precess in phase following a RF pulse. Alternatively, it represents the loss of magnetization in the xy-plane. T_2 relaxation or decay is due to random magnetic interactions that occur between proton spins. It depends on the presence of static internal fields in the substance, generally due to protons in larger molecules. These stationary or slowly fluctuating magnetic fields create local regions of increased or decreased magnetic fields, depending on whether the protons align with or against the main magnetic field. Local field non-uniformities cause the protons to precess at slightly different frequencies. Thus following the 90° pulse, the protons lose coherence and transverse magnetization is lost resulting in T_2 relaxation. However, there is also a dephasing effect caused by local field inhomogeneties, and its characteristic time is referred to as T_2* relaxation. These additional dephasing fields come from the main magnetic field inhomogeneity, the differences in magnetic susceptibility among various tissues, chemical shift and gradients applied for spatial encoding [1]. T_2* is always faster than the T_2 decay **(Figure 1.1 (B))**.
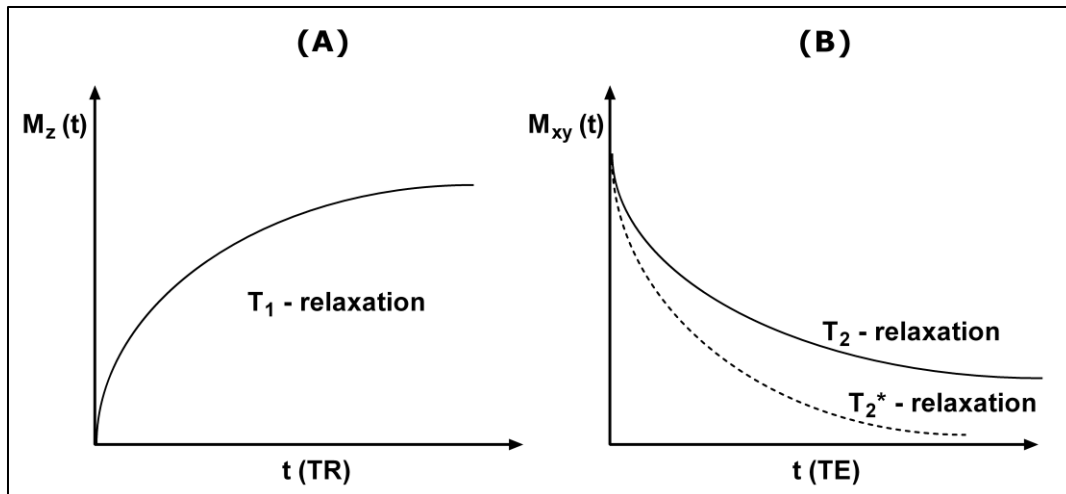
Figure 1.1. Diagram depicting exponential curves of **(A)** T_1 and **(B)** T_2 , T_2* relaxation.

Unlike T_1 interactions, the T_2 interactions do not involve a transfer of energy but only a change in phase, which leads to a loss of coherence. The transverse component of the magnetization precessing around the z-axis emits radio-waves at the Larmor frequency which are then detected and sampled by the receiver.

1.3   Pulse Sequences

MR image contrast allows one to tailor the imaging study to the anatomic part of interest and to the disease being studied. Variable MR image contrast is usually achieved by using different pulse sequences and by changing the imaging parameters. Some of the adjustable sequence parameters are the echo time (TE) which is the time from excitation to sampling and the repetition time (TR) which is the time elapsed between the two excitations. In general, a T_1-weighted sequence uses a short TR and a short TE (TR < 1000msec, TE < 30msec). With the choice of long TE and long TR the images become T_2-weighted (TR > 2000msec, TE > 80 msec).

There are various pulse sequences, however spin-echo is the most commonly used sequence. This sequence includes a slice selective 90degree excitation RF pulse followed by one or more 180 degree refocusing RF pulses. The inversion recovery pulse sequence is normally used to give heavy T_1-weighting. This sequence includes a 180 degree RF pulse that inverts the magnetization followed by a 90 degree RF pulse that brings the residual longitudinal magnetization into the x-y or transverse plane where it is then detected by an RF coil. This sequence makes signal nulling possible. For example, the fluid-attenuated inversion recovery (FLAIR) produces heavily T1-weighted images but cancels the signal coming from CSF. This type of sequence proves to be particularly

useful in the detection of subtle changes at the periphery of the hemispheres and in the regions close to CSF.

1.4 T_2 Mapping

T_2 weighted sequences usually suffer from several problems including signal intensity variability caused by coils and motion artifacts. T_2 mapping is a quantitative technique which can be used to overcome the previously mentioned limitations. T_2 maps are generated by fitting (mono- (Eqn.1) or bi- exponential (Eqn.2)) following Bloch equation, where *'t'* correspond to different T_2 weighted scans obtained using different TE's or echo times.

$$M_{echo} = M_0 \exp(-t / T_2) \dots\dots\dots\dots\dots \quad (1)$$

$$M_{echo} = M_{0(long)} \exp(-t / T_{2(long)}) + M_{0(short)} \exp(-t / T_{2(short)}) \dots\dots\dots\dots \quad (2)$$

To determine T_2 we solve the above equations using least square fit for M_{echo} by determining the slope of the intensity plot vs. *t*. The value of T_2 obtained from a single exponential fit usually represents an average value of the MR signal coming simultaneously from relaxation of protons in different environments and it does not account for different relaxation rates in different portions of the curve. Whereas the bi-exponential fitting operation splits the MR signal obtained from the same study into two components accounting for different relaxation rates present within the same voxel. The first component is associated with the voxels with a long or high T2 values and the second component is associated with the voxels with a short or low T_2 values. So, a bi-exponential function permits best of the data, giving information about the voxels

5

associated with high and low T_2 values within the same study. The following example **Figure 1.2.** represents the M0 maps and the corresponding residual sum of squares map obtained using mono- and bi-exponential fitting of T_2 weighted images acquired at 28 echo points.
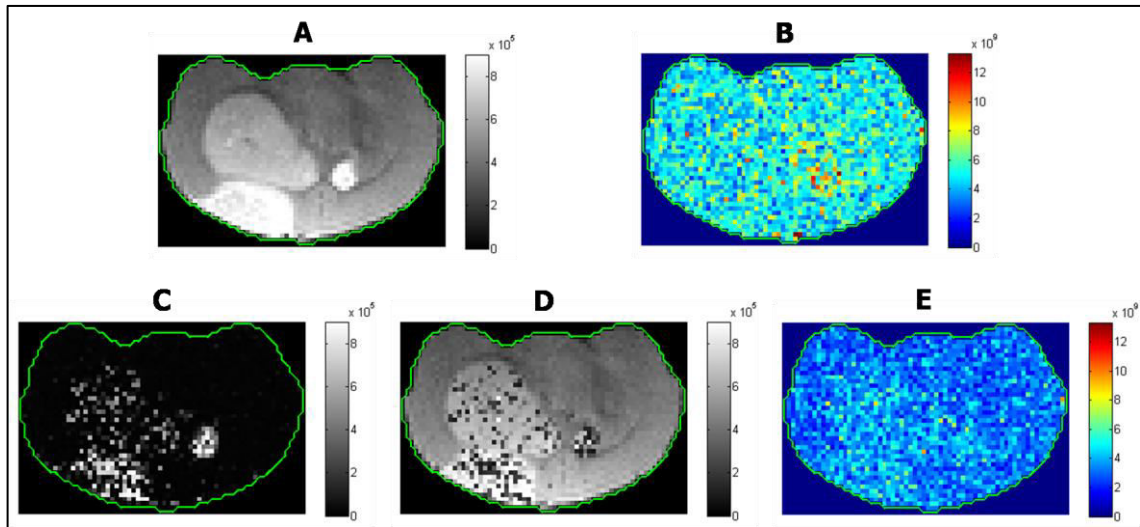
Figure 1.2. Figure representing (A) M0 map obtained from mono-exponential fitting; (C), (D) M0-High and M0-Low maps obtained from bi-exponential fitting respectively; (B), (E) Residual sum of squares map for mono- and bi- exponential fitting respectively. Note, the residual sum of square map for bi-exponential fitting has lower values compared to mono-exponential fitting indicating a perfect fit using bi-exponential equation.

1.5 Diffusion Imaging

Diffusion weighted imaging or diffusion tensor imaging is a form of MR imaging which is based upon the diffusion of water molecules within a voxel (it is a combination of "volume" and "pixel" where pixel is a single picture element of an MR image). The MR image contrast in a DTI is derived from differences in the motion of water molecules between tissues which is related to the micro-environment of the tissue. This technique is specifically sensitive to the self-diffusion of intracellular water molecules present in the

sample being imaged. The molecular diffusion is based upon the thermally driven random Brownian motion of water molecules in a fluid environment. The movement of molecules is represented by the diffusion coefficient (D), which depends on the viscosity of the media, size of the molecules and temperature. In an unrestricted environment, like water kept inside a glass, the diffusion is isotropic i.e. equal in all directions **(Figure 1.3 (A))**, whereas the
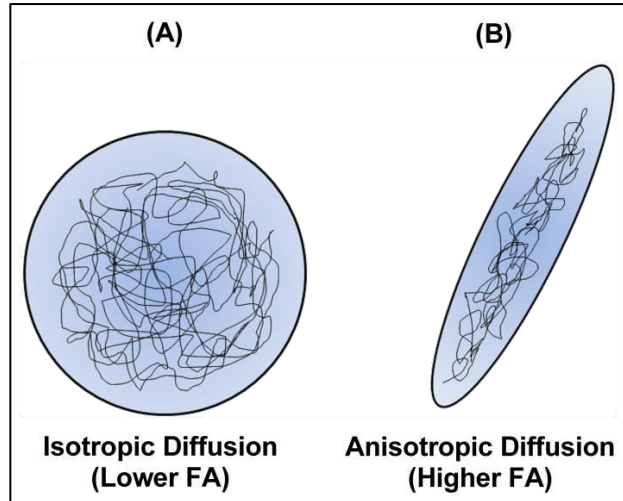
Figure 1.3. Schematic illustration of **(A)** isotropic diffusion (molecular displacements in all directions) with a lower FA values, and **(B)** diffusion (greater molecular diffusion in a particular direction) with higher FA values. The diffusion is anisotropic due to anatomical barriers causing diffusion to be restricted perpendicular to the fibre direction.

diffusion is unequally restricted in different directions or is anisotropic **(Figure 1.3 (B))** in the case of a biological tissue due to movement of water molecules by organelles and the cell membrane. Therefore, in biological tissues the calculated diffusion is termed as Apparent Diffusion Coefficient (ADC).

The DWI is based on the EPI spin-echo sequences in which pairs of diffusion sensitizing gradient pulses are applied. In a basic DWI, the diffusion is measured along three orthogonal directions providing diffusion weighted images or ADC maps. However, to obtain the information about the directional dependence of the diffusion signal, the DTI technique is used, which allows the diffusion to be considered in 3D. This technique requires a larger number of diffusion sensitizing gradient pulses or diffusion directions

(minimum of 6), which causes phase shifts of the protons along the direction in which they are applied. The gradient pulses are usually applied with time interval of 20ms to 50ms during which the phase refocuses perfectly in the absence of molecular diffusion. However, in the presence of molecular diffusion the phase does not refocus perfectly resulting in an attenuated MR signal. The observed attenuation in the signal is then used to build a tensor representation of the diffusion and to estimate the diffusion coefficient in each direction. In this model, the diffusion tensor is characterized by the length and direction of three major axes, which can be visualized as an ellipsoid, where the axes represent the three principal diffusion orientations or eigenvectors (v_1, v_2, v_3) and corresponding diffusion coefficients or eigenvalues (λ_1, λ_2, λ_3). The degree to which diffusion is directionally dependent can be expressed as fraction anisotropy (FA). This parameter can be calculated from the eigenvalues using equation **I**. FA takes values from 0 to 1 representing isotropic and anisotropic diffusion respectively. Apparent diffusion coefficient of ADC can be calculated using equation **II**.

$$FA = \sqrt{\frac{(\lambda_1 - \lambda_2)^2 + (\lambda_1 - \lambda_3)^2 + (\lambda_2 - \lambda_3)^2}{2(\lambda_1^2 + \lambda_2^2 + \lambda_3^2)}} \quad \dots\dots\dots\dots\dots\dots\dots\dots\dots\dots\dots\dots\dots \text{(I)}$$

$$ADC = \frac{\lambda_1 + \lambda_2 + \lambda_3}{3} \quad \dots\dots\dots\dots\dots\dots\dots\dots\dots\dots\dots\dots\dots\dots\dots\dots\dots\dots\dots \text{(II)}$$

For more information on the principles of MRI and diffusion imaging, reader is referred to textbooks on this subject viz. *Principles of magnetic resonance imaging: a signal processing perspective* and *Diffusion MRI: From Quantitative Measurement to In vivo Neuroanatomy* [2, 3].

2. IMAGE PROCESSING

2.1   Image Segmentation

Segmentation is an important technique used for dividing an image into meaningful structures and is often an essential step in image analysis. In the segmentation process the pixels sharing similar characteristics are assigned a unique label which results in a mask for that respective region of interest. Each of the pixels in the defined region share similar properties, such as color, intensity or texture and the adjacent pixels outside the region are significantly different with respect to the same characteristics. Based on different technologies, there are three general approaches to segmentation, termed threshold-based, edge-based methods and region-based methods.

Threshold based segmentation

Thresholding is probably the most frequently used technique to segment an image. It is based on partitioning an image into the regions that are similar to predefined criteria. The thresholding technique can be defined by following operation.

$$g(x,y) = \begin{cases} 1 & if \quad f(x,y) > T \\ 0 & if \quad f(x,y) \le T \end{cases}$$

where, T is the selected threshold value; g(x,y) is thresholded output image (binary image); f(x,y) are original gray level image pixel values and x,y are the pixel coordinates in the image.

The thresholded output is a mask or a binary image with pixel values of 1 and 0. The pixels with values above the selected threshold from the original gray scales image

takes the value 1 in the generated output mask. This mask when multiplied with the original image provides the segmented image, in which, all the pixel values inside the mask remains same as original image where as outside it is zero. **(Figure 2.1)**
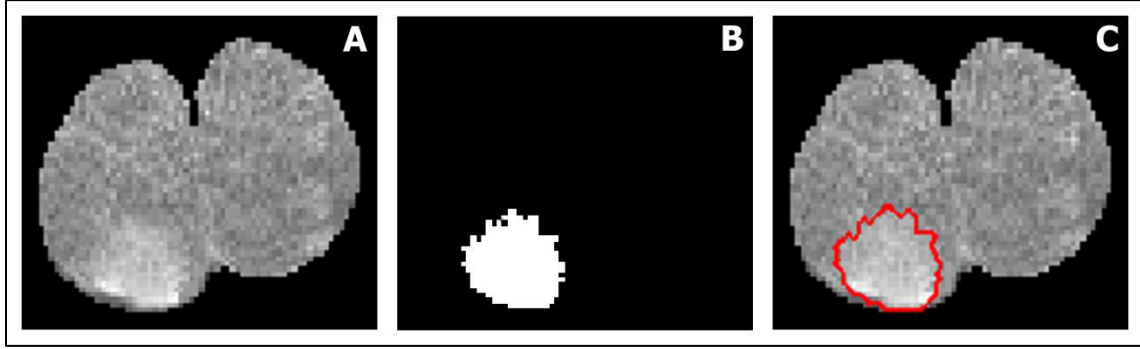
Figure 2.1. Figure illustrating segmentation through thresholding. (A) MR T_2-weighted image, (B) Mask generated after thresholding, (C) The segmented region is represented with-in red contour.

k-means clustering

k-means is an unsupervised iterative problem and it is based on the intuition that a dataset with *n* observations or data-points can be partitioned into *k* clusters in which each observation belongs to the cluster with the nearest mean.

The algorithm tries to minimize the average squared Euclidean distance of *n* data-points from their cluster centers. The cluster center is defined as the mean or centroid μ_j of the data-points in a cluster S_j.

$$L = \sum_{j=1}^{k} \sum_{i=1}^{n} || x_i - \mu_j ||^2$$

where, x_i is a vector representing the nth data point and μ_j is the geometric centroid of the data points in S_j.

In k-means algorithm we try to minimize the L quantity through following steps:

a. Initialize means μ_1, μ_2 ... μ_k randomly in the dataset as centers of K clusters.

b. Assign each point to the nearest mean by calculating the distance from the data point to each cluster.

c. If the data point is closest to its own cluster, leave it where it is without updating the mean. If the data point is not closest to its own cluster, move it into the closest cluster and update the mean to the center of its cluster.

Iterate steps (b) and (c) until convergence i.e. until a complete pass through all the data points results in no data point moving from one cluster to another.

<u>Steps for applying k-means algorithm for image segmentation</u>

i. Specify a value for *k*.

ii. Vectorize the input image.

iii. Obtain different pixel values present in the image with their frequency. (Generate histogram).

iv. Select random μ_1, μ_2 ... μ_k centroids.

v. Compute the distances of each pixel value from the selected centroids and obtain the minimum. Assign the pixel value to k^{th} cluster, where μ_k is the nearest centroid.

vi. Compute the means for each cluster and update the centroids.

vii. If the updated centroids are same as the previous centroids the algorithm ends, else, repeat steps (vi) and (viii).

viii. Obtain the mask for the image by assigning each pixel value to a kth cluster, where μ_k is the nearest centroid.

For MATLAB implementation of the above algorithm refer Appendix I.

Region Growing

It is a simple region based image segmentation method. In this technique the first step is usually to select a set of seed points based on some user criterion (for example, pixels in a certain gray-level range). The regions are then grown from these seed points (**Figure 2.2(A)**) to adjacent points based on the difference between a pixel's intensity value and the region's mean which is then further compared with the threshold set by the user. The pixel with the smallest difference i.e. less than the threshold, is allocated to the region. This process is carried until the intensity difference between region mean and the new pixel becomes larger than the threshold. **Figure 2.2(B)** represents the final segmented region after region growing.

For MATLAB implementation of the above algorithm refer to Appendix I.
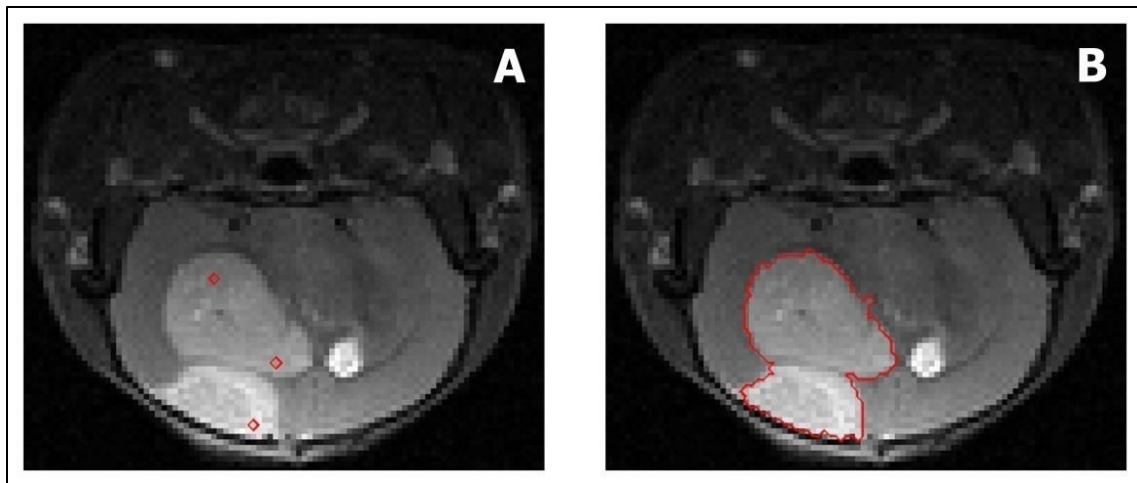
Figure 2.2. Region growing algorithm implementation for the segmentation of tumor on a T_2-weighted MR image. (A) Figure showing the initial seeds (*red dots*). (B) Figure showing the final segmented tumor image. Threshold was set to a value of 0.11*(region mean).

Level set based segmentation

In level set methods, a contour of interest is represented as a zero level set of a higher dimensional function, called a level set function (LSF), and the motion of this contour is formulated as the evolution of the LSF. The curve evolution can be expressed as $(\partial C(s,t))/\partial t = FN$, where F is the speed function that controls the motion of the contour, and N is the inward normal vector to the curve C. In level set formulation the dynamic contour $C(s,t)$ is embedded as the zero level contour of a time dependent LSF $\Phi(x,y,t)$. The embedding LSF Φ takes negative values inside the zero level contour and positive values outside. The normal inward vector can be express as $N = \nabla\Phi \,/\, |\nabla\Phi|$, where ∇ is the gradient operator. The curve evolution can be converted to partial differential equation (PDE), also referred to as level set equation, $\partial\Phi/\partial t = F\,|\nabla\Phi|$.

The main advantage of level set methods is that they can represent contours of complex topology and are able to handle topological changes, such as splitting and merging. In level set formulations, the LSF is typically initialized and periodically reinitialized as a signed distance function. The level set evolution can be represented as an equation for gradient flow as follows:

$$\frac{\partial\Phi}{\partial t} = \mu \left[\nabla^2\Phi - \mathrm{div}\left(\frac{\nabla\Phi}{|\nabla\Phi|}\right)\right] + \lambda\delta_\varepsilon(\Phi)\mathrm{div}\left(g\frac{\nabla\Phi}{|\nabla\Phi|}\right) + \alpha g\delta_\varepsilon(\Phi)$$

(a)   (b)   (c)

In the above equation, the first term on the right hand side is associated with the distance regularization energy **(a)**, while the second and third terms are associated with the external energy terms. The energy functional term **(b)** is minimized when the zero level contour Φ is located at the object boundaries. The energy functional term **(c)** is

introduced to speed up the motion of the zeros level contour in the level set evolution process. λ and α are the coefficients of the energy functional terms **(a)** and **(b)** respectively. A nonzero α value gives additional extra force to drive the motion of the contour. For Images with weak object boundaries a larger value of α causes the active contour to pass through object boundaries (boundary leakage). So, for images with weak boundaries, the value of α should be chosen relatively small to avoid boundary leakage. The level set evolution is less sensitive to parameters λ and μ, so, they can be fixed for most of applications. In the algorithm the value of λ and μ are set to a value 5 and (0.2 / Timestep) respectively. The parameter Timestep determines the speed of the evolution curve as per the following equation:

$$\Phi^{k+1} = \Phi^k + Timestep * \frac{\partial \Phi}{\partial t}$$

where, Φ^k and Φ^{k+1} are the initial and updated contour (LSF) respectively during the curve evolution process.

Further, the description of variables used in the above equation are as follows :

δ_ε , is the Dirac delta function defined as,

$$\delta_\varepsilon(x) = \begin{cases} \frac{1}{2\varepsilon}\left[1 + \cos\left(\frac{\pi x}{\varepsilon}\right)\right], & |x| \leq \epsilon \\ 0, & |x| \geq \epsilon \end{cases}$$

The parameter epsilon or ε is the width of the Dirac delta function and is usually set to a value of 1.5.

g, is the edge indicator function defined as,

$$g = \frac{1}{1 + |\nabla G_\sigma * I|^2}$$

where, G is the Gaussian kernel with a standard deviation σ. I is the input image. The convolution in the edge indicator function is used to smooth the image so as to reduce the noise. The function *g* usually takes smaller values at the object boundaries that at the other locations.

For further detailed information about the implementation and formulations of level set algorithm, the reader is requested to refer to the research paper "*Distance Regularized Level set Evolution and Its Application to Image Segmentation*" *by Chunming Li and Chenyang Xu.* For MATLAB implementation of the above algorithm refer to Appendix I.

2.2   Image Registration

Image registration is an automatic or manual process of overlaying two different images so as to spatially align them on a common coordinate system. In medical image analysis it is a vital step which allows to study and compare two or more images of the same scene taken at different times, or from different viewpoints. Registration algorithms compute transformations to set correspondence between the two images.

In this paper b-spline grid based image registration technique was implemented. In this technique a grid of b-spline control points is constructed which controls the transformation of the input image. An error measure is then used to compute the registration error between the two images.

For implementation, the MATLAB algorithm *"B-spline Grid, Image and Point based Registration"* by Dirk-Jan Kroon was used. The user can obtain the above algorithm freely from the web. In the initial step of this algorithm the user has to select the landmarks / corresponding points in the two images which are then used as reference points for the registration. The MATLAB algorithm for the selection of these initial points along with the main function is included in the Appendix I.

3. MRI STUDY OF TRAUMATIC BRAIN INJURY

3.1   Introduction

Traumatic brain injury (TBI) is one of the most common neurologic disorders and a leading cause of disability affecting independence, productivity and quality of life and as a result is an important public health problem in United States [4-6]. The most recent estimates of the incidence and prevalence of TBI in USA, indicate that annually 50,000 deaths, 1.1 million are treated in emergency departments and 235000 are hospitalized for nonfatal TBI [7]. TBI is usually caused due to shear forces of impact on head, initiating complex biological mechanisms and tissue atrophy. The heterogeneity of resulting TBI pathology is considered to be one of the most significant barriers to finding effective therapeutic treatments [8, 9]. Primary injury occurs immediately due to the mechanical insult and is generally followed by delayed secondary injury events leading to alterations in cell function and propagation of injury which accounts for many of the post-TBI neurological deficits [10-12]. Development of secondary injury processes potentially provides a time frame for therapeutic intervention, which can be utilized to devise therapies for preventing the progressive tissue atrophy and improving the long-term recovery of the function [13, 14].

To date, the knowledgebase for TBI pathology has been obtained largely from regional tissue measurements using histological and immuno-histological methods at a single time point (terminal) analysis. Such methods do not allow dynamic assessment of tissue abnormalities [15]. Hence, non-invasive characterization of the damage extent is very essential to establish effective neuro-protective treatments. Non-invasive

characterization of the injury microenvironment is often difficult to achieve through conventional neuroimaging methods (CT, MRI (e.g. T_1w and T_2w)) as they are not sensitive enough to identify regions undergoing micro-structural changes [16-19]. However, MRI quantitative techniques (e.g. Diffusion weighted and T_2 maps) are proved to be a highly sensitive and valuable tool in the study of TBI, providing crucial information about the spatio-temporal developments of the tissue damage along with added insights into the disease mechanisms [17, 20, 21]. Magnetic resonance Diffusion Tensor Imaging (DTI), including calculation of the apparent diffusion coefficient (ADC) and Fractional anisotropy (FA) are found helpful in distinguishing between cytotoxic and vasogenic edema [22-26] and are shown to be correlated well with the injury severity [27-30].

TBI model of controlled cortical impact (CCI) used in the present study, involves a rigid impact or that produces the mechanical energy onto the dura with the head of the animal kept restrained during the impact [31, 32]. The key advantage of this model includes the ability to control deformation parameters such as time, velocity and depth of the impact. This model is used to mimic whole spectrum of focal-type damage and diffuse axonal injury [33].

The objective of this work was to acquire the prognostic information at early stages of TBI in rats using Diffusion Tensor Imaging (DTI) and quantitative mapping of T_2 relaxation properties by identifying the regions undergoing micro-structural changes from 24-hours to 7-days post injury. Further, to verify the MRI findings, the obtained quantitative MRI information was correlated with the immuno-histochemistry data.

3.2 Materials and Methods

3.2.1 *Model*

Arizona State University's Institute of Animal Use and Care Committee (IACUC) approved all procedures described in this study. Traumatic brain injury (TBI) was modeled with the well- established controlled cortical impact (CCI) injury models (Impact One; Leica Biosystems, IL) [32]. Briefly, Adult Long Evans Hooded male rats (245-265 g; n = 15) were anesthetized with isoflurane (5% induction, 2% maintenance) and placed in stereotaxic frame. The fronto parietal cortex was exposed via 5mm craniotomy. The impactor tip diameter was 3 mm, the impact velocity was 4.0 m/s and the depth of cortical deformation was 2 mm. Low viscosity composite Wave (SDI limited, Bensenville, IL) was applied and light cured for 20 seconds, casing the craniotomy and the impact site after the injury. The skin was sutured and the animals were placed in an incubator (37°C) until consciousness was regained. Injured animals were randomly assigned to either 24-hours or 7-days survival group. The sham group had the same surgical procedure, but with no injury and was sacrificed after 7-days (n=3).

3.2.2 *MRI Measurements and Analysis*

Rat brain MRI images were acquired using ParaVision software on a Bruker-Biospin 7-Tesla system with 30 cm bore magnet, (BrukerBiospin, BNI, AZ). A volume transmitter coil (72 mm) was placed inside the magnet for radio frequency excitation, and a rat brain radio frequency (RF) surface coil was used for signal detection. Animals were placed at prone position on a nonmagnetic holder with the teeth bar as an aid to fix the head position. During image acquisition, anesthesia was maintained using isoflurane (1.5%), respiration was monitored using SAII system and rectal temperature was

maintained at 37°C. Each animal was imaged at two time points viz. 24-hours and 7-days after induction of CCI. Diffusion Tensor Images (DTI) were acquired using a spin-echo pulse sequence with repetition time (TR) of 4750 msec and echo time (TE) of 25 msec. Diffusion encoding gradients were applied in six directions using a b-value of 500 s/mm^2. The obtained DTI images were then used to generate Apparent Diffusion Coefficient (ADC) and Fractional Anisotropy (FA) maps in MATLAB (R2012b, The MathWorks, MA) using the equations **I** and **II** (Chapter 1). T_2–weighted images were obtained during the same imaging session and at the same neuro-anatomical level as the diffusion weighted images, using a multislice–multiecho pulse sequence with TR = 6000 msec and TE = 22 msec. All the images were acquired with the following acquisition parameters: number of slices, 19; slice thickness, 0.5 mm; interslice distance, 0.5 mm; field of view 30 x 30 mm; matrix dimensions 192 x 192 (resulting in 156 x 156 µm in plane resolution). The T_2 maps were generated using the ParaVision software with TEs of 22, 44, 66, 88, 110, 132, 154, 176, 198, 220 msec and TR of 6000 msec with the same field of view, matrix size and slice number as T_2–weighted images.

The rat brains were segmented by manually outlining the ipsilateral and contralateral hemispheres. To analyze and quantify the MR parameters, two regions of interests (ROIs) were selected on the injured brain slices of the 24-hours and 7-days T_2 map images. The lesion or injury area (ipsilateral ROI) was identified on the ipsilateral hemisphere using the threshold of mean plus one-standard deviation of T_2 values in the contra-lateral hemisphere of the same brain slice. Obtained ROIs were then flipped on to the corresponding contralateral hemispheres of the same rat brain slice. Flipping operation ensured that the contralateral ROI generated is of the same size and at the same

anatomical location as the ipsilateral ROI. These ROIs were then saved and transferred to corresponding slices of ADC and FA maps and the mean, standard deviation, and number of pixels for each ROI was extracted. The mean values were obtained by averaging the pooled means (the average of all the pixel intensities inside the selected ROIs, computed across all the slices) of individual parametric map for each rat. To compare the variations in the MR parametric maps, the pooled means obtained from the contralateral ROIs are used as the control and were plotted against the pooled means of the ipsilateral ROIs. To study the injury evolution and the volume comparison, 24-hours MR images and 7-days histological sections were registered to the 7-days MR images using the non-rigid transformation and B-spline grid manual warping methods. Calculation of injury volume was computed by multiplying the number of voxels inside the ipsilateral ROI of each slice by the slice thickness and resolution of the image. All analysis and quantification of MR data was performed using MATLAB (R2012b, The MathWorks, MA).

3.2.3   *Immunohistochemistry Measurements and Analysis*

According to the experimental groups - 24-hours and 7-days post-injury, the animals were deeply anesthetized with sodium pentobarbital until a tail pinch produced no reflex movement. Animals were transcardially perfused with cold Phosphate-Buffered Saline (PBS), followed by 4% buffered paraformaldehyde solution. Brain samples were removed and fixed overnight in 4% buffered paraformaldehyde followed by immersion in 30% sucrose solutions in 1X PBS for cryoprotection for 24-hours. Samples were embedded within optimal cutting temperature medium and frozen on dry ice. Samples were stored at -80°C until sectioned on a Leica CM3050 S Cryostat (Leica Microsystems, Buffalo Grove, IL). Serial cryosections (16μm thick) were collected between 3.70 mm

anterior and -0.40 mm posterior to Bregma were used for analysis. The sections were placed on subbed (positively charged) glass slides; with two sections per slide and were stored at -80°C.

For measurements, the slides containing the frozen sections were first equilibrated in -20°C for 15 minutes and then at room temperature for another 20 minutes in 1X PBS. Sections were permeabilized with 0.5% Triton X-100 and blocked in PBS containing 4% horse serum for an hour. Monoclonal mouse IgG glial fibrillary acidic protein, GFAP (Millipore;Billerica, MA, USA) and polyclonal rabbit IgG CD68 (Abcam;Cambridge, MA, USA) was used to double stain the slides. The primary antibodies, mouse anti-GFAP (1:250 dilution) and rabbit anti-CD68 (1:100 dilution) was diluted using 0.2% Triton X-100 and 2% horse serum with PBS and were incubated overnight at 4°C. After washing with 1X PBS, the sections were incubated with appropriate secondary antibodies, Alexa Fluor 555 goat anti-mouse IgG (Invitrogen; Carlsbad, CA, USA; 1:200 dilution) and 488 goat anti-rabbit IgG (Invitrogen; 1:200 dilution), for 2 hours at room temperature. Sections were then washed in PBS buffer. DAPI (Invitrogen; 1 µl/1000 µl) was diluted with 1X PBS and was incubated for 10 minutes. Anti-fading media and coverslip were applied, after the sections were washed with PBS. A negative control was included with the same procedure as above, except for use of the primary antibodies (instead 1X PBS was used).

Immunostained sections were imaged using Leica DMI 6000B (Leica Microsystems, Buffalo Grove, IL; 10X magnification). The images were analyzed using MATLAB (R2012b, The MathWorks, MA). The program used a threshold value

(background value plus one standard deviation) specific to each stain to remove the background stain of the images. In order to quantify the positive GFAP and CD68 stains; the pixel values above the threshold values in the background-subtracted images were considered. Another program was used to quantify the total area of brain tissue by manually drawing ROIs to select the ipsilateral and the contralateral hemispheres of the brain sample. Total pixel values within the each ROI were considered as the total area of each hemisphere. The positive GFAP and CD68 were then expressed as a percentage of the total brain tissue.

3.2.4 *Statistics*

Statistical analyses were performed using Prism v6 (GraphPad, CA) with statistical significance level set to a p-value of 0.05. One-way Analysis of Variance (ANOVA) was used to test the significance between the results obtained for MRI data at each time point. If significance was noticed, the means were compared using unpaired student's t-test to assess the differences within the group. Paired student's t-test was then used to compare the observed means at each time point for each subject. Linear Regression was used to model and observe the relationship between the obtained 24-hours and 7-days post injury MRI results. To analyze IHC, the percentage of astrocytes and macrophages for each time point was statistically compared by two-tailed t-test.

3.3   Results

Changes in MR signal in TBI animals were noticed in the T_2, ADC and FA parametric maps as deviations in the pixel intensities at both the time points.

At 24-hours post TBI, high intensity pixel values were observed at the lesion site on the T_2 maps with a mean of 76.59 ± 5.5 msec and had a significant difference from the mean T_2 value (51.95 ± 1.6 msec) of the control ROIs *(P <0.0001)*. By 7-days, increase in the T_2 values were noted for most of the animals indicating formation of edema, (mean T_2 of 94.70 ± 27.7 msec) and was statistically significant from the control mean T_2 *(P<0.001)*, **Figure 3.1(A), Table 3.1**. However, no significant difference was observed between the 24-hours and 7-days ipsilateral (lesion) T_2 values. The lesion volumes were found to be 25.83 ± 12.2 mm^3 at 24-hours which was considerably reduced to 3.73 ± 2.7 mm^3 by 7-days *(P<0.001)*. Furthermore, a significant correlation was observed between the 24-hours and 7-days T_2 values (R2 = 0.86, *P< 0.05*, slope = 4.7 ± 0.83), and the lesion volumes (R2 = 0.59, *P<0.05*, slope = 0.17 ± 0.06), **Figure 3.2(A), 3.2(B)**. The slopes and the Y intercept of the volumes at 24-hours provide a good prediction of injury observed at day-7.

Table 3.1. Mean values of T_2, ADC and FA parameter maps with statistical comparisons between ipsilateral and contralateral region of interests at 24-hours and day-7 post TBI. [1]

		Ipsilateral	vs. Contralateral
T_2	24-hours	76.6 ± 5.49	52.0 ± 1.67, *(P<0.0001)*
	day-7	94.7 ± 27.7	49.4 ± 2.41, *(P<0.001)*
ADC $(x10^{-3})$	24-hours	0.94 ± 0.14	0.83 ± 0.04
	day-7	1.83 ± 0.51	0.81 ± 0.07, *(P<0.0002)*
FA	24-hours	0.51 ± 0.08	0.60 ± 0.05, *(P<0.05)*
	day-7	0.46 ± 0.07	0.60 ± 0.13, *(P<0.05)*
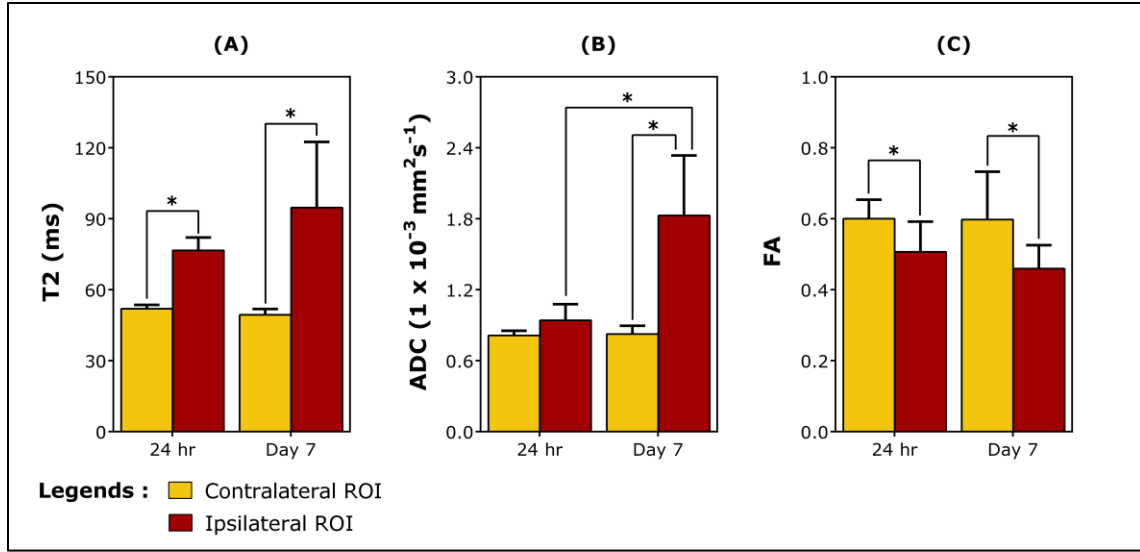
Figure 3.1. Quantitative T_2 (A), ADC (B) and FA (C) values of the ipsilateral and contralateral ROIs observed at the 24-hours and day-7 post injury. Note that there was no statistical difference between the ipsilateral and contralateral ROIs for ADC values on 24-hours post TBI. Data presented here as mean ± SD, (* *P <0.05*).
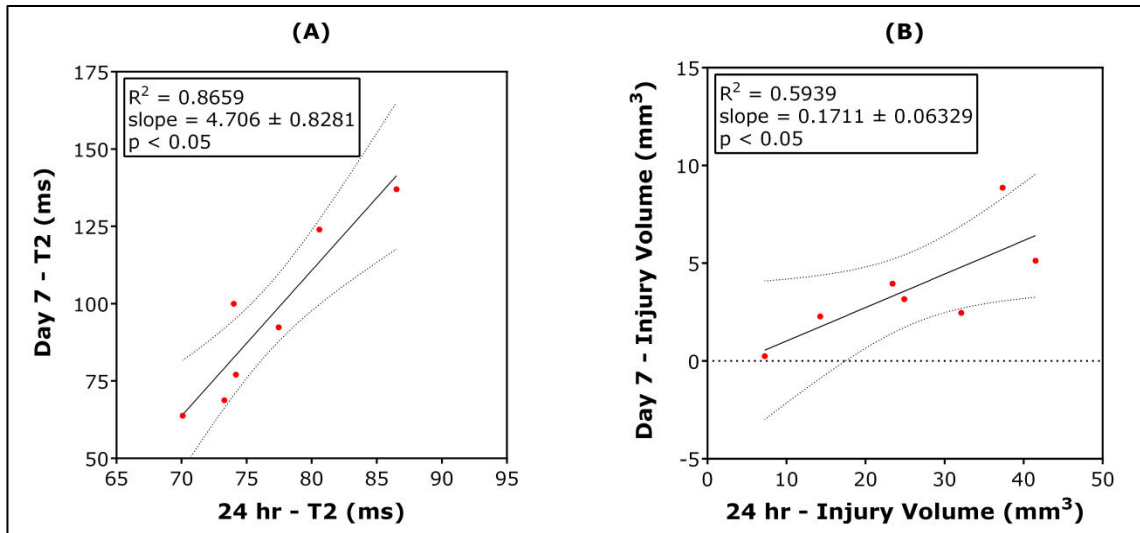
Figure 3.2. Whole group correlations between 24-hours and day-7 observations of **(A)** T2 values (*P <0.05*, R^2 = 0.7616, slope = 3.404); and **(B)** Lesion Volumes (*P <0.05*, R^2 = 0.7128, slope = 0.2327).

25

The mean apparent diffusion coefficient (ADC) and fractional anisotropy (FA) values were calculated from the diffusion maps across ipsilateral and contralateral ROIs as detailed under methods section. At 24-hours post TBI, both hyper-intensity and hypo-intensity pixels were observed in the ipsilateral ROIs on the ADC maps. Unlike the T_2 maps, this anomaly in pixel intensities was unique to ADC maps **(Figure 3.3(C))** and had no significant differences between the
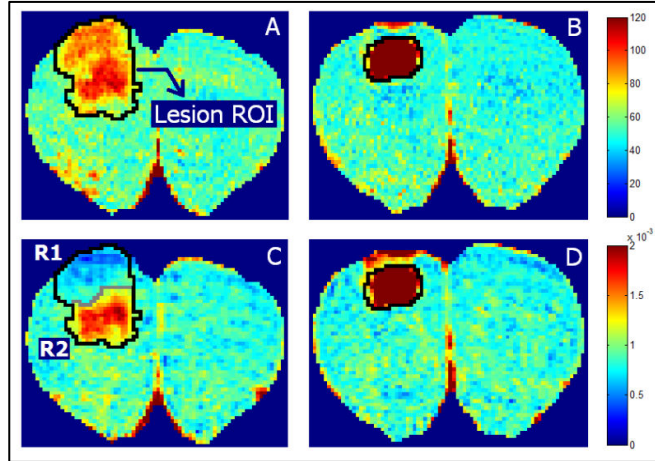
Figure 3.3. T2 (*A and B*) and ADC (*C and D*) maps of a single slice from a representative animal at 24-hours and 7-days post injury respectively. At 24-hours homogenous hyper-intensity pixels were observed through-out the lesion ROI in T_2 map **(A)** when compared to ADC map **(C)**; **R1** (Sub-region-1) and **R2** (Sub-region-2) corresponds to the hypo- and hyper-intensity region respectively. At 7-days only hyper-intensity pixels were observed in both T_2 **(B)** and ADC **(D)** maps.

mean ADC values of lesion (0.94 ± 0.14 x10^{-3}) and control regions (0.83 ± 0.04 x10^{-3}), **Figure 3.1(B)**. However, 7-days after injury, hypo-intensity pixels were not detected and statistically significant ADC hyper-elevations were observed between the ROIs (lesion: 1.83 ± 0.51 x10^{-3}; control: 0.81 ± 0.07 x10^{-3} , *P<0.0002*). For further analysis of the 24-hours ADC maps, the area within the ipsilateral ROI was segmented into two regions using the threshold as mean plus 2 standard-deviations of the pixel intensities in the control ROIs. The proximal or hypo-intensity region (pixel values below the threshold) was labeled as Sub-region-1 (**R1**) where as the distal or hyper-intensity region (pixel values above the threshold) was labeled as Sub-region-2 (**R2**), **Figure 3.3**.

Interestingly, when the sub-regions were compared with the control values at 24 hours post injury, a significant difference was observed only for the distal (hyper-intensity) region **R2** (1.3 ± 0.12 x10^{-3}, *P <0.0001*), indicating the ADC values in the proximal region **R1** approximately equal to that of normal ADC values, **Figure 3.4(B)**. This deviation in the ADC pixel intensity values between the regions highly correlated with the observed deviation in the FA values at 24-hours. It was observed that the mean FA values were significantly higher *(P <0.05)* in the proximal region (0.56 ± 0.13) compared to that of the distal region (0.41 ± 0.11), **Figure 3.4(C)**. Using registration techniques, the sub-regions **R1** and **R2** obtained from the 24-hour ADC maps were transferred on to the day-7 T_2, ADC and FA maps. It was observed that the day-7lesion area significantly overlaps with the proximal region (overlap $\approx$ 72%) and the T_2 and FA pixel values in the distal region reduce to control values, marking the resolution of the injury **(Figure 3.4(C))**. For mean values of sub-regions refer **Table 3.2**.

Table 3.2. Mean values of T_2, ADC and FA parameter maps with statistical comparisons between contralateral region of interest, sub-region 1 and sub-region 2 at 24-hours and day-7 post TBI.

|		Contralateral ROI	vs. Sub-region 1 (R1) (Proximal)	vs. Sub-region 2 (R2) (Distal)
T_2	24-hours	52.0 ± 1.67	78.2 ± 8.67, *(P<0.0001)*	79.0 ± 5.65, *(P<0.0001)*
	day-7	49.4 ± 2.41	59.1 ± 7.95, *(P<0.01)*	54.4 ± 6.56
ADC ($x10^{-3}$)	24-hours	0.83 ± 0.04	0.73 ± 0.12	1.30 ± 0.12, *(P<0.0001)*
	day-7	0.81 ± 0.07	1.12 ± 0.18, *(P<0.002)*	0.94 ± 0.11, *(P<0.05)*
FA	24-hours	0.60 ± 0.05	0.56 ± 0.13	0.41 ± 0.11, *(P<0.002)*
	day-7	0.60 ± 0.13	0.58 ± 0.06	0.64 ± 0.08
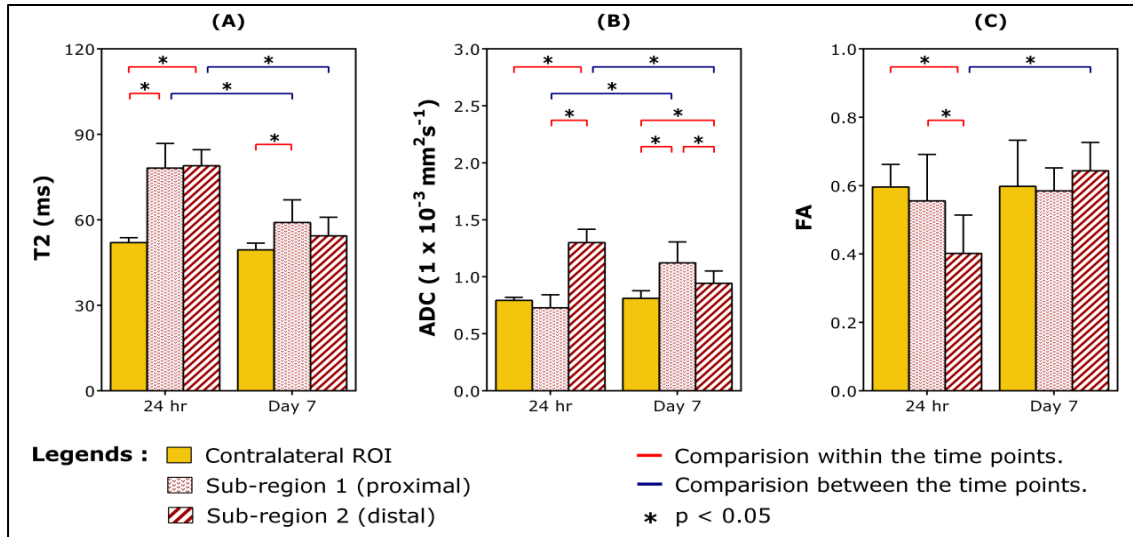
Figure 3.4. Quantitative T2 (A), ADC (B) and FA (C) values of the sub-regions (R1 and R2) and contralateral ROIs observed at the 24-hours and 7-days post injury. Note that compared to 24-hours, at 7-days no significant differences were observed between the Sub-region 2 and contralateral ROI for quantitative T_2, ADC and FA values, indicating the resolution of the injury within the distal region ($p > 0.5$).

Histological Results

The GFAP positive stain significantly increased in the ipsilateral hemisphere as compared to the contralateral hemisphere for both 24-hours and day-7 time points **(Figure 3.5(A), and 3.6)**. The reactive astrocytes, marked by GFAP, were activated on 24-hours of injury and sustained through day-7 post TBI. There was no significant increase in the ipsilateral hemisphere from 24-hours to day-7 time point. However, the CD68 activation significantly increased at day-7 as compared to 24-hours **(Figure 3.5(B), 3.6)** near the injury site. The histological evidence of tissue damage correlated well with the observed MR signal changes. The MRI at day-7 detected the brain contusion and edema as markedly increased T_2, ADC and decreased FA values. This observation was associated with the regions of cavity or the grossly visible tissue loss on the histological sections **(Figure 3.6)**.

28
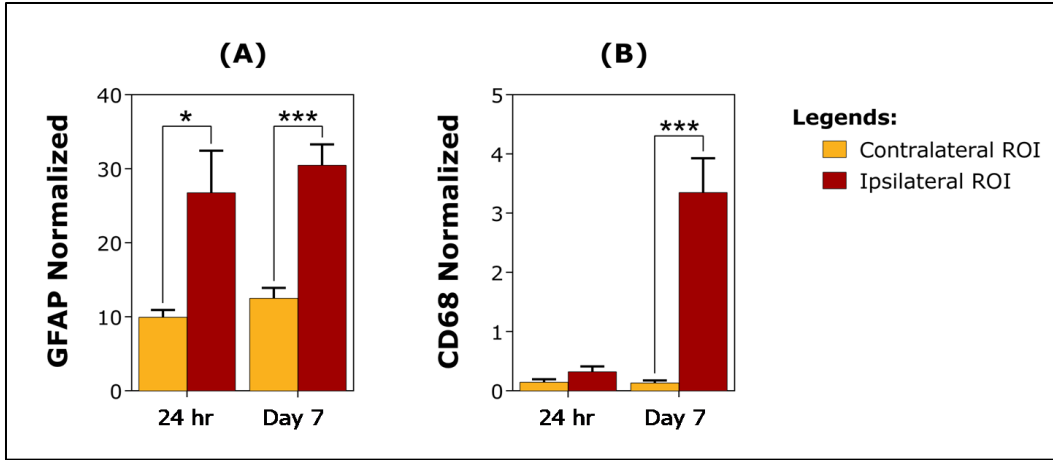
Figure 3.5.(A) Quantification of GFAP (astrocyte marker) positive GFAP expressed as a percentage of the total brain tissue. *p<0.05, ***p<0.0001; **(B)** Quantification of CD68 (microglia/macrophage marker) positive CD68 expressed as a percentage of the total brain tissue. ***p< 0.0001.
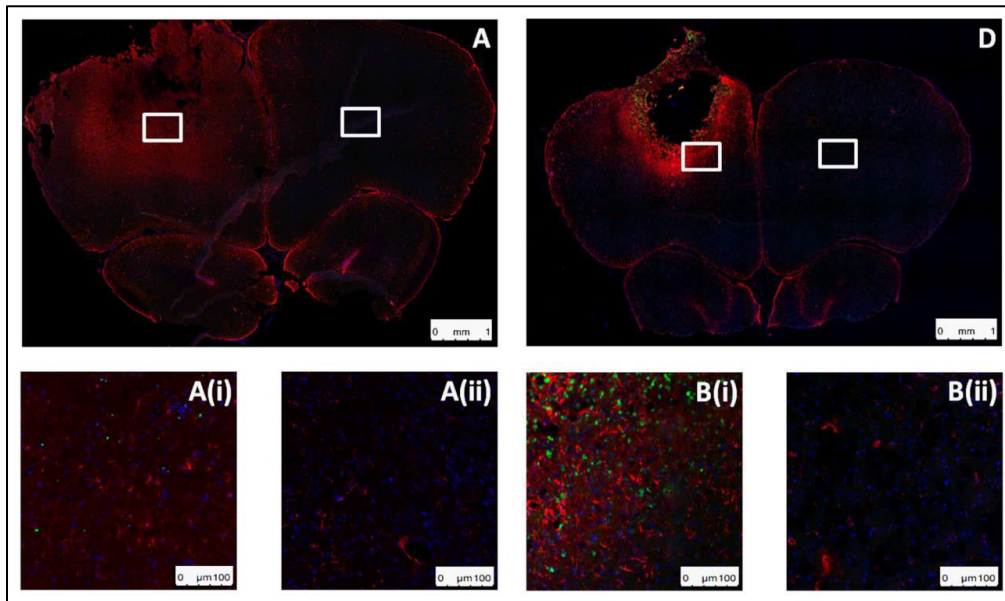
Figure 3.6. Representative IHC images of injured rat brain (A) 24 hours and (B) 7 days post injury. The zoomed in view of ipsilateral and contralateral hemisphere are shown in A(i), B(i) and A(ii), B(ii) respectively. Color code: GFAP in red, CD68 in green and DAPI in blue.

3.4   Discussion

The present study examined the temporal evolution of quantitative MR signal changes from 24-hours to 7-days post TBI (induced by controlled cortical impact) and then was compared to histology evaluations. The MR imaging techniques provide potential information on the viability of the brain tissue. The quantitative mapping technique especially DTI is very sensitive to micro-structural alterations and has been found to reveal TBI lesions that are not visible by conventional MRI [24, 28, 34, 35].

In the present study, regions of hyper-intensities were observed at 24-hours after trauma on the T_2 map images with a 50% increase above the normal T_2 values. These hyper-intense T_2 pixel values were mainly associated with the hemorrhage caused due to the mechanical impact during trauma [36, 37]. Contrasting to T_2 maps, pixel values on ADC maps were associated with hyper- and hypo-intensities within the same TBI lesion. The decrease in ADC values reflects decreased water diffusion which was mainly associated with the cytotoxic edema; where cytotoxic edema is caused by the disruption in the cellular metabolism impairing the functioning of the sodium (Na) and potassium (K) ion pumps in the glial cell membrane leading to cellular retention of Na and water where water mobility is restricted [25]. This was highly supported with the observed FA results depicting high anisotropy values in the hypo-intensity regions of the ADC **(Figure 3.4(C))**. Interestingly, these hypo-intensity regions were observed near the contusion site, which eventually deteriorated into the injury observed on 7-days, with significantly higher T_2 and ADC values compared to control. In contrast, the pixels in the hyper-intensity region at 24-hour ADC maps resolved to normal values by 7-days as observed in all the quantitative parametric maps **(Figure 3.4)**. There was approximately a two-fold

increase in the ADC and an 80% increase in the T_2 values compared to control on day-7 lesion sites. This observed increase in T_2 and ADC at 7-days was found to be associated with a decrease in tissue cellularity (disrupted cells) and cavity formation, usually attributed to vasogenic edema [25, 26]. These areas of hyper-intensity give a good correlation with the lesion size as obtained from the histology. The T_2 hyper-intensity and early decrease in ADC observed at 24-hours followed by increased diffusion by 7-days post trauma was in agreement with other experimental MRI findings [27, 38-40].

The cerebral hemodynamic abnormality after TBI generally includes three stages: hypo perfusion (during the day of the injury), hyperemia (during the next 3 days), and vasospasm (lasting the next 2 weeks/thereafter) [41]. The activation of microglia and astrocytes and the infiltration of circulating monocytes can be important sources of toxic substances including proinflammatory cytokines [42]. *I hypothesize that the activated astrocytes may be a critical contributing factor for elevation in T_2 at 24-hours* (**Figure 3.1, 3.5(A)**). Increased edema and breakdown of the extracellular matrix occur due to increased vascular permeability, leads to progressive vascular injuries [42]. Microglial cells marked by CD68 get fully activated where the tissue damage is extensive. Focal TBI typically results in the rapid accumulation of microglia/macrophages within the cortical penumbra, with activated microglia surrounding the cortical contusion, which is thought to promote tissue degeneration and repair [43]. In a study on inflammation after ischemia, it was found that at early times the CD68 was confined in the border zone of the lesion and at day-7 it increased greatly, and invaded the ischemic core [44], which correlates well with our study (**Figure 3.5(B), 3.6**). *I also hypothesize that expression of CD68 plays a role in the elevation in ADC on day-7* (**Figure 3.1, 3.5(B)**).

4. MRI STUDY OF BRAIN TUMOR

4.1   Introduction

Dendritic cells (DC) are the master regulators of the adaptive immune response in the human body, and much effort has been focused upon the development of these specialized cells to be used in stem cell based vaccine therapy. In the 17 years that have elapsed since the publication of the first DC vaccine therapy trial, much progress has been made toward the goal of using DC as a legitimate vaccine therapy approach for the treatment of cancers. A clinical review of 38 Glioblastoma (a type of brain tumor) patients by Wheeler et al. found that patients vaccinated with DC prior to chemotherapy exhibited significantly longer two year overall survival (OS) (42%) than patients treated with either vaccination or chemotherapy alone (8%). Additional review of 20 DC-based vaccine trials for the treatment of brain tumors also has indicated some potential successes. Cho et al. demonstrated that addition of DC vaccine pulsed with protein, to standard of care therapy for newly diagnosed Glioblastoma doubled OS to 31.9 months (n=18) in comparison to contemporary controls (n=16) who did not receive the vaccine (OS = 15.0 months). Ardon et al. vaccinated 45 pediatric patients with relapsed brain tumors including three patients with Atypical Teratoid Rhabdoid Tumor (ATRT). The patients with relapsed ATRT had responded most favorably to DC vaccination. Two were alive at 34.1 and 52.6 months of follow-up and the third had died of disease at 50.5 months post vaccination. Hence, stem cell vaccine therapy has engendered a certain degree of optimism in the ability of certain brain tumors to be treated by these methods.

4.2   Materials and Methods

4.2.1   *Tumor Model*

A mouse glioma model using mouse glioma GL261 cells was tested in this study. A total of 12 female, C57/Black6 mice were used. The mice were divided into 2 cohorts with 6 mice in each cohort. In order to administer the 'DC vaccine' to the mice cohorts, 20 additional mice were used to collect spleen and bone marrow for dendritic cell (DC) differentiation. These 20 mice were euthanized by standard procedure using isoflurane and by cervical dislocation. The spleen and bone marrow were harvested separately in Hank's Balanced Salt Solution (HBSS). The adherent cells were then differentiated to form mature DCs by addition of mouse cytokines such as GM-CSF (50ng/mL), IL-4 (10ng/mL), IL-1β (10ng/mL), IL-6 (15ng/mL), TNF-α (10ng/mL), PGE2 (1μg/mL). The mature DCs were further primed and made into a 'DC vaccine' by adding RNA and cell lysate from the mouse glioma cells (GL261). Standard IACUC approved protocols were followed for all mice. All mice cohorts were monitored for weight or behavior changes and imaged to assess tumor burden on day 3 and then every subsequent week after tumor cells implantation. All 12 mice were implanted with 500,000/5μL GL261 cells cranially after administering approved anesthetic and antibiotic in order to induce tumor growth. For the treatment, 3 mice from cohort 2 received a single dose of 5-Azacytidine drug and the rest 3 mice received 3 doses of the same drug every week. The remaining 6 mice from cohort 1 were used as an untreated control group. All animals were sacked according to approved protocols after tumor burden was assessed and imaged.

4.2.2 *Measurements and Analysis*

The mice brain MR images were acquired using ParaVision software on a Bruker-Biospin 7-Tesla system with 30 cm bore magnet, (BrukerBiospin, BNI, AZ). A volume transmitter coil (72 mm) was placed inside the magnet for radio frequency excitation, and a rat brain radio frequency (RF) surface coil was used for signal detection. Animals were placed at prone position on a nonmagnetic holder with the teeth bar as an aid to fix the head position. During image acquisition, anesthesia was maintained using isoflurane (1.5 %), respiration was monitored using SAII system and rectal temperature was maintained at 37°C. Each animal was imaged at day-3 post tumor implantation, followed by an interval of 7-days till they lost a significant body weight (after that they were sacrificed). Diffusion Tensor Images (DTI) were acquired using a spin-echo pulse sequence with repetition time (TR) of 3750 msec and echo time (TE) of 18 msec. Diffusion encoding gradients were applied in six directions using a b-value of $1500s/mm^{2}$. The obtained DTI images were then used to generate Apparent Diffusion Coefficient (ADC) and Fractional Anisotropy (FA) maps in MATLAB (R2012b, The MathWorks, MA) using equations I and II (refer Chapter 1). T_2–Weighted images were obtained during the same imaging session and at the same neuro-anatomical level as the diffusion tensor images, using a multislice–multiecho pulse sequence with TR = 4768msecat28 echo points or TE's of 10, 21, 31, 42, 52, 63, 74, 84, 95, 105, 116, 126, 137, 148, 158, 169, 179, 190, 200, 211, 222, 232, 243, 253, 264, 274, 285, 296. The single and multi-parametric T2 maps were then obtained for each slice with the same field of view and matrix size as T_2 weighted images.

All the images were acquired with the following acquisition parameters: number of slices, 15; slice thickness, 0.5 mm; interslice distance, 0.5 mm; field of view 30 x 30 mm; matrix dimensions 128 x 128 (resulting in 150 x 150 µm in plane resolution).

For the analysis, the mice brains were automatically segmented by k-means clustering and level-set evolution algorithms followed by a manual visual check. To analyze and quantify the MR parameters three region of interest's (ROI's) were selected on the T_2 weighted MR image slices, where a visual evidence of the tumor was observed. The ROI-1 outlined the tumor region observed on the T_2-weighted image slices for each mice and it was obtained using region-growing algorithm (a region-based image segmentation method). The ROI-2 outlined the peri-tumoral region which was 2-pixelswide (300 micrometers) surrounding the tumor ROI. The ROI-3 was used as a control and it outlined the contralateral hemisphere. All the ROI's were visually checked and it was made sure that the CSF (Cerebrospinal Fluid) was excluded (**Figure 4.1**). The obtained ROI's were then saved and transferred to corresponding slices of T_2, ADC, FA and M_0 maps and then the mean, standard deviation, and number of pixels for each ROI was extracted. The pooled means (the average
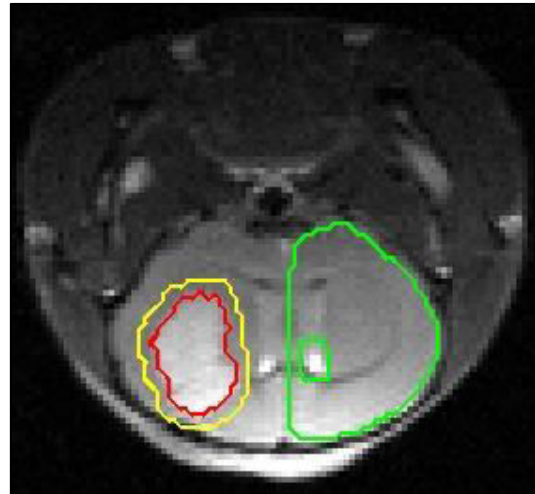
Figure 4.1. T_2 weighted single image slice from a representative animal depicting the three region of interests outlined for the analysis. ROI-1 (*within red*), ROI-2 (*between yellow and red*), and ROI-3 (*within green*) outlined the tumor, peri-tumoral and contralateral regions respectively.

of all the pixel intensities inside the selected ROIs, computed across all the slices) were obtained for individual parametric map, for each slice and for each mice. Calculation of the tumor volumes was computed by multiplying the number of voxels inside the tumor ROI of each slice by the slice thickness and resolution of the image. All analysis and quantification of MR data was performed using MATLAB (R2012b, The MathWorks, MA).To compare in-between cohort variations of the quantitative MR parameters, the pooled means obtained for tumor and peri-tumoral regions for each mice within the same cohort were averaged and then plotted against the averaged pooled means of the corresponding cohort's contralateral ROI's, which was used as a control.

4.2.3 *Statistics*

All results were expressed as mean ± SD. The differences in tumor volumes and variations in MR signal intensities in-between the region of interests and different cohorts were analyzed by one-way ANOVA, followed by the Students t-test. All statistical analyses were performed using Prism v6 (GraphPad, CA). The level of significance was set at $P < .05$.

4.3   Results

Cohort 1 with no vaccine control

In Cohort 1 (n=6) no tumor was identified in any of the mice at 3-days post tumor implantation. Out of 6 mice, only one mice survived till 31 days post tumor implantation. The tumor volume and quantitative MR values of that mice were not considered for statistical comparisons and the related values are represented in **Figure 4.2(A)** and **Figure 4.3(1A-4A)** respectively. Follow-up imaging showed an increase in tumor

36

volumes where tumors significantly grew after 17 days (0.35 ± 0.26 at day-10, 4.28 ± 2.57 at day-17 vs. 34.83 ± 23.7 at day-24, *P <0.001, <0.002* respectively), **Figure 4.2(A)**. High intensity pixels were observed at the lesion (tumor) site on the T_2, ADC and M_0-fraction parameter maps at day-10, 17, and 24 and were found significantly different when compared to the mean values of contralateral and peri-tumoral regions of respective maps on corresponding days **(Table 4.1)**. Only T_2 values at day-10 showed a significant change between peri-tumoral and contralateral regions *(P <0.002)*.The deviation in FA values between the regions of interest were comparable with the observations in T_2 and ADC maps. Low intensity pixels were observed at the lesion site on the FA maps at post day-3 images, but were found significantly different from the mean values of contralateral and peri-tumoral region only at day-24 (Contralateral: 0.44 ± 0.04, Peri-tumoral: 0.51 ± 0.04 vs. Tumor: 0.36 ± 0.03, *P <0.01, <0.0001* respectively). Interestingly, at day-24 the FA mean values of peri-tumoral region was found significantly higher compared to the contralateral region *(P <0.03)*, **Figure 4.3**.
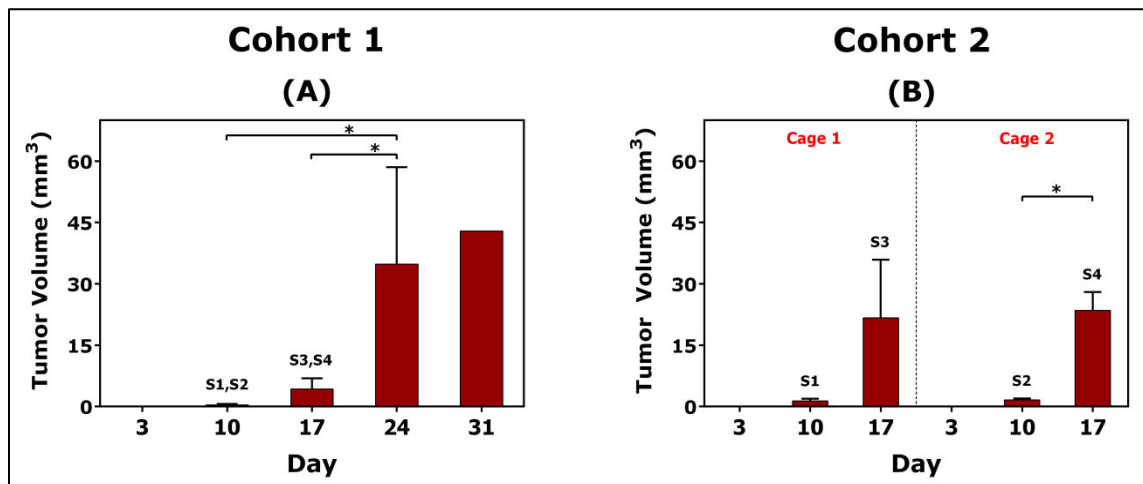
Figure 4.2. Tumor volumes observed for (A) cohort-1 and (B) cohort-2 (Cage-1 and Cage-2).

Table 4.1. Mean values of T_2, ADC and M_0-fraction parameter maps with statistical comparisons between Tumor, Contralateral and Peri-tumoral regions of interest for Cohort 1.

		Tumor	**vs. Contralateral**	**vs. Peri-tumoral**
T_2	day-10	51.7 ± 1.65	49.9 ± 1.04, *(P<0.03)*	47.1 ± 1.00, *(P<0.0001)*
	day-17	61.7 ± 4.57	49.4 ± 0.96, *(P<0.0001)*	49.9 ± 1.67, *(P<0.0001)*
	day-24	64.1 ± 2.27	49.9 ± 0.97, *(P<0.0001)*	51.7 ± 1.12, *(P<0.0001)*
ADC	day-10	0.70 ± 0.03	0.61 ± 0.02, *(P<0.0001)*	0.59 ± 0.02, *(P<0.0001)*
	day-17	0.81 ± 0.06	0.60 ± 0.01, *(P<0.0001)*	0.62 ± 0.02, *(P<0.0001)*
	day-24	0.88 ± 0.05	0.61 ± 0.02, *(P<0.0001)*	0.65 ± 0.04, *(P<0.0001)*
M_0-Fraction	day-10	0.09 ± 0.03	0.05 ± 0.00, *(P<0.002)*	0.05 ± 0.00, *(P<0.002)*
	day-17	0.20 ± 0.04	0.04 ± 0.01, *(P<0.0001)*	0.05 ± 0.01, *(P<0.0001)*
	day-24	0.22 ± 0.03	0.05 ± 0.01, *(P<0.0001)*	0.08 ± 0.03, *(P<0.0001)*

Compared with day-10 a significant increase in T_2, ADC and M_0 lesion mean values were observed at day-17 and at day-24 (T_2: *P <0.0001, <0.0001,* ADC: *P <0.001, <0.0001,* M_0-fraction: *P<0.0001, <0.0001* respectively), however only ADC lesion mean values at day-24 were significantly different compared to day-17 *(P < 0.05)*. In peri-tumoral region a significant increase in T_2 mean values was observed at day-17 and day-24 compared with day-10 (*P<0.003, <0.001* respectively) and also day-24 T_2 mean values were found significantly higher than the day-17 (*P <0.05*). ADC and M_0-fractionperi-tumoralmean values showed a significant increase at day-24 compared to day-10 (ADC: *P<0.01*; M_0-fraction: *P<0.01*) and only M_0-fraction peri-tumoral mean values were significantly increased by day-24 compared with day-17 (*P< 0.05*). **Table 4.1.**

Cohort 2 with vaccine control

Cohort-2 (n=6) was divided into two sub-groups based on the applied doses of drug for the treatment. Cage-1 (n=3) mice were given only a single dose of vaccine at day-3 post tumor implantation where as cage-2 (n=3) mice were given 3 doses of vaccine every week post tumor implantation. Compared to cohort-1 the cohort-2 (cage-1 and cage-2) mice survived for only 17 days post tumor implantation and no tumor was detected at day-3. A significant increase in tumor volumes was observed at day-17 compared to day-10 only for cage-2 *(P <0.002)*, and the tumor volumes at day-10 and day-17 were comparable between the two cages **(Table 4.3)**, **Figure 4.2(B)**. Significantly high intensity pixels were observed at the lesion site compared to the contralateral and peri-tumoral regions on the T_2, ADC and M_0-fraction parameter maps at day-10 and day-17 for both the cages **(Table 4.2)**. Only T_2 values of cage-1 mice at day-10 showed a significant change between peri-tumoral and contralateral regions *(P <0.05)*. On the cage-1 and cage-2 FA parameter maps, significantly low intensity pixels were observed at the lesion site compared to contralateral and peri-tumoral regions at day-10 and day-17 **(Table 4.2)**. Besides, the peri-tumoral FA values were significantly higher compared to contralateral region at day-10 for cage-1 *(P <0.006)* and at day-17 for cage-2 *(P <0.02)*. Further, a significant increase in cage-2 peri-tumoral FA values was observed from day-10 to day-17 *(P <0.05)*, **Figure 4.3(3B)**.

Statistical comparisons between cohort 1 and cohort 2

The tumor volumes of cohort-1 were significantly lower from both the cage-1 and cage-2 compared at day-17 **(Table 4.3)**. Also, a significant change was observed between cohort-1 and cage-2 ADC mean values at day-17 *(P <0.05)*.

Table 4.2. Mean values of T_2, ADC and M_0-fraction parameter maps with statistical comparisons between Tumor, Contralateral and Peri-tumoral regions of interest for Cohort 2.

		Tumor	vs. Contralateral	vs. Peri-tumoral
T_2 (Cage-1)	day-10	52.9 ± 0.72	48.5 ± 0.67, *(P<0.0001)*	46.3 ± 0.82, *(P<0.0001)*
	day-17	61.7 ± 3.75	48.4 ± 0.66, *(P<0.0001)*	50.2 ± 0.31, *(P<0.0001)*
T_2 (Cage-2)	day-10	54.0 ± 2.15	48.3 ± 0.48, *(P<0.0001)*	47.9 ± 0.53, *(P<0.0001)*
	day-17	63.9 ± 4.16	48.8 ± 0.29, *(P<0.0001)*	51.7 ± 2.05, *(P<0.0001)*
ADC (Cage-1)	day-10	0.74 ± 0.02	0.59 ± 0.00, *(P<0.0001)*	0.57 ± 0.01, *(P<0.0001)*
	day-17	0.81 ± 0.05	0.56 ± 0.02, *(P<0.0001)*	0.59 ± 0.03, *(P<0.0001)*
ADC (Cage-2)	day-10	0.73 ± 0.03	0.60 ± 0.01, *(P<0.0001)*	0.60 ± 0.01, *(P<0.0001)*
	day-17	0.88 ± 0.03	0.59 ± 0.01, *(P<0.0001)*	0.62 ± 0.07, *(P<0.0001)*
M_0-Fraction (Cage-1)	day-10	0.15 ± 0.02	0.04 ± 0.00, *(P<0.0001)*	0.04 ± 0.01, *(P<0.0001)*
	day-17	0.24 ± 0.08	0.04 ± 0.00, *(P<0.0001)*	0.06 ± 0.02, *(P<0.0003)*
M_0-Fraction (Cage-2)	day-10	0.11 ± 0.02	0.04 ± 0.01, *(P<0.0001)*	0.04 ± 0.01, *(P<0.0001)*
	day-17	0.23 ± 0.06	0.05 ± 0.01, *(P<0.0001)*	0.06 ± 0.02, *(P<0.0003)*
FA (Cage-1)	day-10	0.30 ± 0.02	0.36 ± 0.00, *(P<0.03)*	0.44 ± 0.02, *(P<0.0001)*
	day-17	0.33 ± 0.03	0.41 ± 0.03, *(P<0.02)*	0.48 ± 0.03, *(P<0.0003)*
FA (Cage-2)	day-10	0.33 ± 0.04	0.39 ± 0.02, *(P<0.03)*	0.41 ± 0.04, *(P<0.006)*
	day-17	0.34 ± 0.04	0.42 ± 0.06, *(P<0.03)*	0.50 ± 0.01, *(P<0.0002)*

Table 4.3. Statistical comparisons between Cohort 1 and Cohort 2 (cage 1 and cage 2) mean tumor volumes.

	Cohort 1	vs. Cage 1	vs. Cage 2
day-10	0.35 ± 0.26	1.33 ± 0.55	1.56 ± 0.39
day-17	4.28 ± 2.58	21.65 ± 14.3, *(P<0.0002)*	23.53 ± 4.48, *(P <0.0001)*
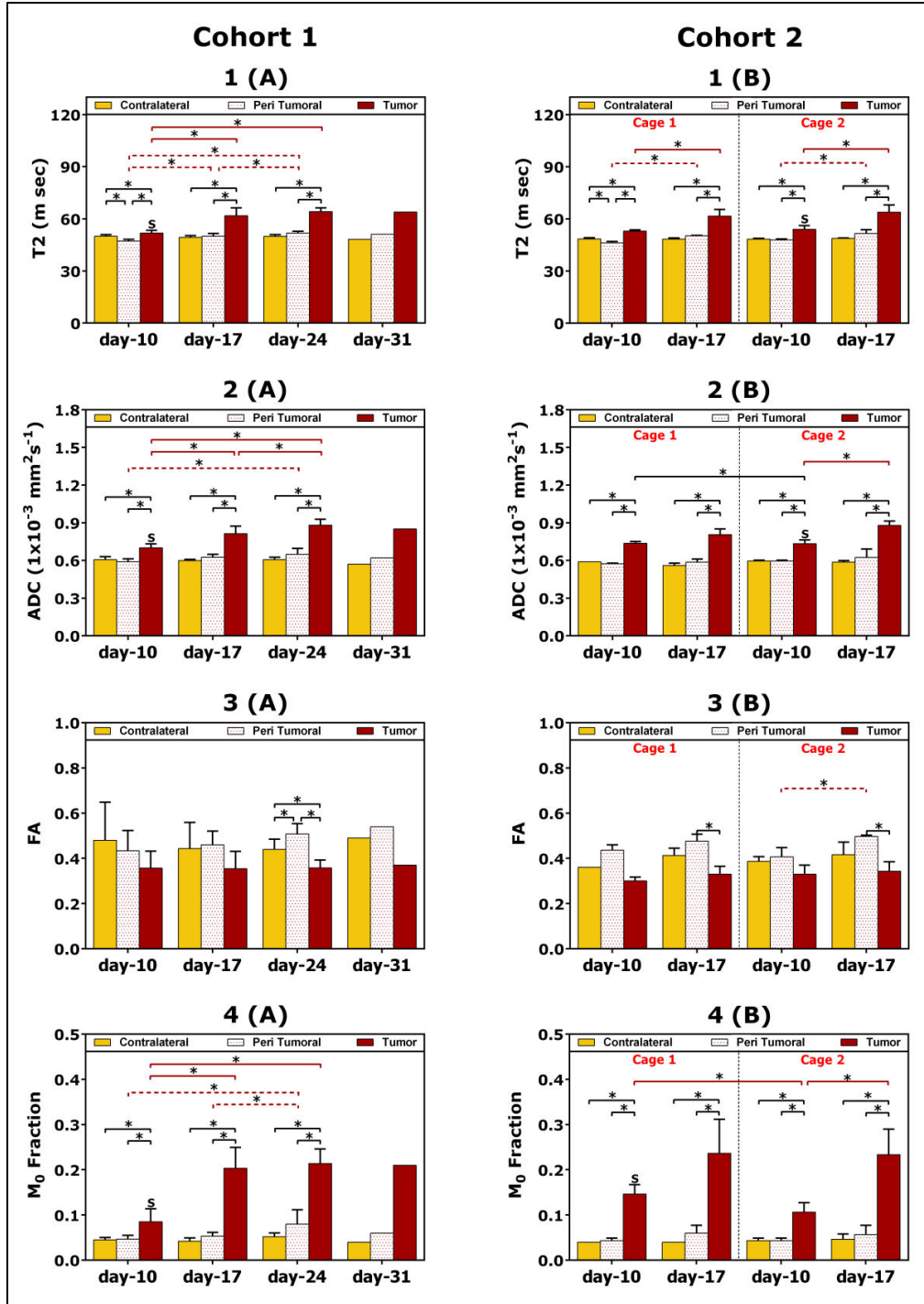
Figure 4.3. Quantitative T_2: **1(A), 1(B)**; ADC: **2(A), 2(B)**; FA: **3(A), 3(B)** and M_0-fraction: **4(A), 4(B)** mean values of the contralateral, peri-tumoral and tumor ROIs observed at the post day-3 tumor implantation for the two cohorts. Data presented here as mean ± std (*$P < 0.05$*). Note, Cohort 2 is divided into two groups based on the doses of drug applied, represented as Cage 1 (single dose) and Cage 2 (multiple doses).

4.4   Discussion

Accurate assessment of tumor response to treatment for each individual patient is crucial in determining whether to continue the current therapy or switch to an alternative therapy [45-47]. The measurements in tumor volume changes play an important role during the assessment and is a critical component for the evaluation of therapeutic efficacy as it is often related to patient survival length. Further, the MR parameters T_2, ADC and FA are shown to be a sensitive marker of tumor response to anticancer treatments [48-50].

In the present study, The MRI results did not show any significant changes in between the two treated cohorts with no reduction in tumor volumes compared to the control group. The future studies would be focused on issues regarding the optimal dose for the application of DC vaccine.

5. CONCLUSIONS

In this final chapter, the main conclusions of the present thesis project are summarized, and some perspectives of this and related work are outlined. Finally, directions for future studies are proposed.

5.1. Conclusions

In the current MRI study of animal models with severe TBI, significant variations in the parametric T_2, ADC and FA values was noticed at the initial scan of 24 hours as well as at the follow-up scan 7-days post injury. T_2 values tended to be hyper-intense at both the time points representing hemorrhage caused due to the mechanical impact during trauma at 24-hours and cavity formation associated with disrupted cells on day-7. DTI parameters: the ADC and FA values were critical in distinguishing the injury region at 24-hours into cytotoxic and vasogenic edema and in outlining the injury regions resolving to normal values by day-7. While interpretation of non-invasive imaging data should be performed cautiously due to inherent methodological limitations (such as resolution, sample size and lack of exact histological correlates). DTI might provide a prospective tool for the *in vivo* tracking of micro-structural reorganization during recovery from TBI. Together, these quantitative MRI analyses of micro- and macro-structural changes using conventional T_2 and DTI techniques complemented each other in this study of severe TBI. Serial application of these MRI techniques would enable the monitoring of the extent and distribution of biological changes post TBI. In addition to it, DTI may capture biological severity at the micro-structural level and provide prognostic information during the early chronic face of TBI. This project contributed to the evolving research

43

area of advance imaging of TBI in animal models, providing new insight into the possibilities of measuring brain changes quantitatively following TBI.

The second project of this thesis is a pilot study on employing dendritic cell based vaccinations and Azacytidine drug in mice glioma model. In this synergistic study the applied dosage of drug did not show any significant deviation in quantitative MR parameters between treated mice and controls. Further, an increase in volumetric tumor growth was observed in the treated cohorts compared to the control, and the treated mice survived approximately one week less than the controls. The biological reasons for this increased tumor growth rate in the treated cohorts is still unclear and the interpretation is outside the scope of the current quantitative multi-parametric MR study.

5.2. Future Directions

For future studies of TBI, a study with more number of animals are required with different injury severity models, especially in order to determine the diagnostic and potential of DTI technique in TBI. Prospective studies with serial imaging at multiple time points (more than 2) would be extremely critical for following micro- and macro-structural brain changes over time and in translating the results to clinical situations. The, injury severity measurements should be included in the study as it is critical for classification of experimental TBI models into mild, moderate and severe levels. Finally, DTI should be acquired with higher resolution and with more diffusion-encoding directions than in the present study allowing tractography based analysis. The tractography measurements would be of particular interest and presumably unravel more aspects of TBI patho-physiology. With the rapid advancements in the field of imaging,

detailed characterization of injury following TBI, and insights into the cellular and sub-cellular levels during recovery, may ultimately lead to therapeutic improvements.

The next stage of the tumor study presented here would be concentrated on the issues regarding the optimal dose for the application of DC vaccine with an intention to restrict or delay the tumor growth rate in the treated cohorts compared to the control. The quantifiable MR parameters may provide valuable insights into the patho-physiology and treatment response of the tumor. Finally, the image segmentation and registration algorithms developed during this project can be directly applied for analysis and quantification of further imaging data that would be acquired during this larger treatment study.

REFERENCES

1. Chavhan, G.B., et al., *Principles, techniques, and applications of T2*-based MR imaging and its special applications.* Radiographics, 2009. **29**(5): p. 1433-49.

2. Liang, Z.P., et al., *Principles of magnetic resonance imaging: a signal processing perspective*. 2000: SPIE Optical Engineering Press.

3. Johansen-Berg, H. and T.E.J. Behrens, *Diffusion MRI: From Quantitative Measurement to In vivo Neuroanatomy*. 2013: Elsevier Science.

4. Murray, C.J.C. and A.D.A. Lopez, *Global mortality, disability, and the contribution of risk factors: Global Burden of Disease Study*, in *Lancet*. 1997. p. 7-7.

5. Hirtz, D., et al., *How common are the "common" neurologic disorders?*, in *Neurology*. 2007. p. 326-337.

6. Masel, B.E. and D.S. DeWitt, *Traumatic brain injury: a disease process, not an event*, in *J Neurotrauma*. 2010. p. 1529-1540.

7. Corrigan, J.D., A.W. Selassie, and J.A. Orman, *The epidemiology of traumatic brain injury*, in *J Head Trauma Rehabil*. 2010. p. 72-80.

8. Saatman, K.E., et al., *Classification of traumatic brain injury for targeted therapies*, in *J Neurotrauma*. 2008. p. 719-738.

9. Doppenberg, E.M., S.C. Choi, and R. Bullock, *Clinical trials in traumatic brain injury: lessons for the future*, in *Journal of neurosurgical anesthesiology*. 2004. p. 87-94.

10. Greve, M.W. and B.J. Zink, *Pathophysiology of traumatic brain injury*, in *Mt. Sinai J. Med.* 2009. p. 97-104.

11. Werner, C. and K. Engelhard, *Pathophysiology of traumatic brain injury*, in *Br J Anaesth*. 2007. p. 4-9.

12. Marshall, L.F., *Head injury: recent past, present, and future*, in *Neurosurgery*. 2000. p. 546-561.

13. Kumar, A. and D.J. Loane, *Neuroinflammation after traumatic brain injury: opportunities for therapeutic intervention*, in *Brain Behav. Immun.* 2012. p. 1191-1201.

14. Shlosberg, D., et al., *Blood-brain barrier breakdown as a therapeutic target in traumatic brain injury.*, in *Nat Rev Neurol*. 2010. p. 393-403.

15. Wang, S., et al., *Comparison of neurite density measured by MRI and histology after TBI.*, in *PLoS ONE*. 2013. p. e63511.

16. Aribisala, B.S., et al., *Multi-parametric classification of traumatic brain injury patients using automatic analysis of quantitative MRI scans*, in *Proceedings of the 5th international conference on Medical imaging and augmented reality*. 2010, Springer-Verlag. p. 51-59.

17. Galloway, N.R., et al., *Diffusion-weighted imaging improves outcome prediction in pediatric traumatic brain injury*, in *J Neurotrauma*. 2008. p. 1153-1162.

18. Lee, H., et al., *Focal lesions in acute mild traumatic brain injury and neurocognitive outcome: CT versus 3T MRI*, in *J Neurotrauma*. 2008. p. 1049-1056.

19. Mayer, A.R., et al., *A prospective diffusion tensor imaging study in mild traumatic brain injury*, in *Neurology*. 2010. p. 643-650.

20. Kharatishvili, I., et al., *Quantitative T2 mapping as a potential marker for the initial assessment of the severity of damage after traumatic brain injury in rat*, in *Experimental Neurology*. 2009. p. 154-164.

21. Immonen, R.J., et al., *Quantitative MRI predicts long-term structural and functional outcome after experimental traumatic brain injury*, in *NeuroImage*. 2009, Elsevier Inc. p. 1-9.

22. Barzo, P., et al., *Contribution of vasogenic and cellular edema to traumatic brain swelling measured by diffusion-weighted imaging*, in *Journal of neurosurgery*. 1997. p. 900-907.

23. Marmarou, A., et al., *Traumatic brain edema in diffuse and focal injury: cellular or vasogenic?*, in *Acta Neurochir Suppl*. 2006. p. 24-29.

24. Hou, D.J., et al., *Diffusion-weighted magnetic resonance imaging improves outcome prediction in adult traumatic brain injury*, in *J Neurotrauma*. 2007. p. 1558-1569.

25. Koch, S., et al., *Diffusion-weighted Imaging Shows Cytotoxic and Vasogenic Edema in Eclampsia*, in *American Journal of Neuroradiology*. 2001. p. 1068-1070.

26. Doelken, M., et al., *Differentiation of cytotoxic and vasogenic edema in a patient with reversible posterior leukoencephalopathy syndrome using diffusion-weighted MRI*, in *Diagnostic and interventional radiology (Ankara, Turkey)*. 2007. p. 125-128.

27. Obenaus, A. and S. Ashwal, *Magnetic resonance imaging in cerebral ischemia: Focus on neonates*, in *Neuropharmacology*. 2008. p. 271-280.

28. Huisman, T.A.G.M., *Diffusion-weighted imaging: basic concepts and application in cerebral stroke and head trauma*, in *European Radiology*. 2003. p. 2283-2297.

29. Benson, R.R., et al., *Global white matter analysis of diffusion tensor images is predictive of injury severity in traumatic brain injury*, in *J Neurotrauma*. 2007. p. 446-459.

30. Wozniak, J.R., et al., *Neurocognitive and neuroimaging correlates of pediatric traumatic brain injury: a diffusion tensor imaging (DTI) study*, in *Arch Clin Neuropsychol*. 2007. p. 555-568.

31. Lighthall, J.W., *Controlled cortical impact: a new experimental brain injury model*, in *J Neurotrauma*. 1988. p. 1-15.

32.   Dixon, C.E.C., et al., *A controlled cortical impact model of traumatic brain injury in the rat.*, in *Neuropharmacology*. 1991. p. 253-262.

33.   O apos Connor, W.T., A. Smyth, and M.D. Gilchrist, *Animal models of traumatic brain injury: a critical evaluation.*, in *Pharmacology and Therapeutics*. 2011. p. 106-113.

34.   Hergan, K., et al., *Diffusion-weighted MRI in diffuse axonal injury of the brain.* Eur Radiol, 2002. **12**(10): p. 2536-41.

35.   Ezaki, Y., et al., *Role of diffusion-weighted magnetic resonance imaging in diffuse axonal injury.* Acta Radiol, 2006. **47**(7): p. 733-40.

36.   Parizel, P.M., et al., *Imaging findings in diffuse axonal injury after closed head trauma.* Eur Radiol, 1998. **8**(6): p. 960-5.

37.   Ashikaga, R., Y. Araki, and O. Ishida, *MRI of head injury using FLAIR.* Neuroradiology, 1997. **39**(4): p. 239-42.

38.   Albensi, B.C., et al., *Diffusion and high resolution MRI of traumatic brain injury in rats: time course and correlation with histology.* Exp Neurol, 2000. **162**(1): p. 61-72.

39.   Onyszchuk, G., et al., *A mouse model of sensorimotor controlled cortical impact: characterization using longitudinal magnetic resonance imaging, behavioral assessments and histology.* J Neurosci Methods, 2007. **160**(2): p. 187-96.

40.   Van Putten, H.P., et al., *Diffusion-weighted imaging of edema following traumatic brain injury in rats: effects of secondary hypoxia.*, in *J Neurotrauma*. 2005. p. 857-872.

41.   Martin, N.A., et al., *Characterization of cerebral hemodynamic phases following severe head trauma: hypoperfusion, hyperemia, and vasospasm.*, in *Journal of neurosurgery*. 1997. p. 9-19.

42.   Lotocki, G., et al., *Alterations in blood-brain barrier permeability to large and small molecules and leukocyte accumulation after traumatic brain injury: effects of post-traumatic hypothermia.*, in *J Neurotrauma*. 2009. p. 1123-1134.

43.   Ziebell, J.M., et al., *Rod microglia: elongation, alignment, and coupling to form trains across the somatosensory cortex after experimental diffuse brain injury.*, in *Journal of Neuroinflammation*. 2012. p. 247.

44.   Perego, C., S. Fumagalli, and M.-G. De Simoni, *Temporal pattern of expression and colocalization of microglia/macrophage phenotype markers following brain ischemic injury in mice.*, in *Journal of Neuroinflammation*. 2011. p. 174.

45.   Brandes, A.A., et al., *Disease progression or pseudoprogression after concomitant radiochemotherapy treatment: pitfalls in neurooncology.* Neuro Oncol, 2008. **10**(3): p. 361-7.

46.   Clarke, J.L. and S. Chang, *Pseudoprogression and pseudoresponse: challenges in brain tumor imaging.* Curr Neurol Neurosci Rep, 2009. **9**(3): p. 241-6.

47.   Hong, X., et al., *Quantitative multiparametric MRI assessment of glioma response to radiotherapy in a rat model.* Neuro Oncol, 2014. **16**(6): p. 856-67.

48.   Chenevert, T.L., et al., *Diffusion magnetic resonance imaging: an early surrogate marker of therapeutic efficacy in brain tumors.* J Natl Cancer Inst, 2000. **92**(24): p. 2029-36.

49.   Morse, D.L., et al., *MRI-measured water mobility increases in response to chemotherapy via multiple cell-death mechanisms.* NMR Biomed, 2007. **20**(6): p. 602-14.

50.   Hamstra, D.A., A. Rehemtulla, and B.D. Ross, *Diffusion magnetic resonance imaging: a biomarker for treatment response in oncology.* J Clin Oncol, 2007. **25**(26): p. 4104-9.

APPENDIX I

MATLAB IMPLEMENTATION OF IMAGE PROCESSING ALGORITHMS

K-MEANS ALGORITHM

```matlab
function Mask = k_means(Input_Image, k)

Input_Image_Vector = Input_Image(:);

% Avoiding zero and negative values present within the image
Input_Image_Vector = Input_Image_Vector-min(Input_Image_Vector)+1;

    % Computing histogram of the image
Image_Histogram = zeros(1, max(Input_Image_Vector));

for iterate1 = 1:length(Input_Image_Vector)

        Image_Histogram(Input_Image_Vector(iterate1)) =...
                Image_Histogram(Input_Image_Vector(iterate1)) + 1;

end

Pixel_Values =find(Image_Histogram);

Centroids =(1:k) * (max(Input_Image_Vector)/(k+1));% Initialize centroids
k_mean_Vector = zeros(1, max(Input_Image_Vector));

while(1)

  % Iterations continues till stopping criterion has not met

Initial_Centroids = Centroids;

% Computing the distance of each pixel from the centroids and
% obtaining the minimum. assigning the pixel value to a label
% k where k is the index of the nearest centroid.

for iterate2 = 1:length(Pixel_Values)

        Distances = (Pixel_Values(iterate2) - Centroids).^2;
Minimum_Distance = find(Distances == min(Distances));
k_mean_Vector(Pixel_Values(iterate2)) = Minimum_Distance(1);

end
```

```matlab
for iterate3 = 1:k        % Updating centroids

        Temp = find(k_mean_Vector == iterate3);
Centroids(iterate3) = sum(Temp.*Image_Histogram(Temp)) / ...
sum(Image_Histogram(Temp));

end
% Stop iterations if Initial Centroids equals to updated centroids
if Initial_Centroids == Centroids
        break,
    end

end

   Mask = zeros(size(Input_Image));% Generating mask for the image

for rows = 1:size(Input_Image,1)
for cols = 1:size(Input_Image,2)

        Distances = (Input_Image(rows, cols) - Centroids).^2;
Minimum_Distance = find(Distances == min(Distances));

Mask(rows, cols) = Minimum_Distance(1);

end
end

figure, imshow(Mask, [1 k])
end
```

REGION GROWING ALGORITHM

```matlab
function Final_Mask = Region_Growing(InputImage, InitialSeeds, InputThreshold)

% InputImage : Input Image
% InitialSeed  : Initial seeds for the algorithm.
   % InputThreshold   : Set appropriate threshold
   % Final_Mask       : This variable holds the output mask.

InputImage = double(InputImage);
Final_Mask = zeros(size(InputImage)); % Create Mask with zeros

% Neighbors pixel positions for the input seed
NeighbourCheck = [-1,-1; -1,0; -1,1; 0,-1; 0,1; 1,-1; 1,0; 1,1];

   [MaxRows, MaxCols] = size(InputImage);

for runs = 1:size(InitialSeeds, 1)

    Mask = zeros(size(InputImage));
InitialSeed = InitialSeeds(runs,:); % Input Seed for region growing
    Threshold = InputThreshold;

% Initializing region mean equal to the input seed.
RegionMean = InputImage(InitialSeed(1), InitialSeed(2));
Threshold  =RegionMean.*Threshold;

InSeed_Row = InitialSeed(1); % Row coordinate of input seed
InSeed_Col = InitialSeed(2); % Column coordinate of input seed

NewSeeds = [];  % Variable "NewSeeds" hold the new input seeds.
    Temp = 1;      % Temporary Variable

% Region Growing Algorithm begins
while (1)

        Check = size(NewSeeds,1);
for runs2 = 1:Check+Temp

if ~isempty(NewSeeds)
InSeed_Row = NewSeeds(runs2,1);
InSeed_Col = NewSeeds(runs2,2);
else
            Temp = 0;
end
```

54

```matlab
% Checking the neighboring positions for the input seed
for runs3 = 1:8

    InRow = InSeed_Row + NeighbourCheck(runs3,1);
    InCol = InSeed_Col + NeighbourCheck(runs3,2);

    if InRow> 0 &&InRow<= MaxRows&&...
    InCol> 0 &&InCol<= MaxCols&&...
    Mask(InRow, InCol) ~= 1

    if InputImage(InRow, InCol) <= (RegionMean + Threshold) &&...
    InputImage(InRow, InCol) >= (RegionMean - Threshold)

    % Updating Mask
    Mask(InRow, InCol) = 1;
    NewSeeds(end+1, :) = [InRow, InCol];  %#ok<AGROW>

    % Recomputing region mean with updated mask.
    RegionMean = sum(InputImage.*Mask)/sum(Mask);
    end

    end
    end
    end
    NewSeeds(1:Check,:) = [];

    if isempty(NewSeeds)
    break;
    end

end
% Region Growing Algorithm Ends

% Fill holes in the output generated mask. (Optional)
Final_Mask = Final_Mask + imfill(Mask, 'holes');
Final_Mask(Final_Mask> 0) = 1;

end

Final_Mask = imfill(Final_Mask , 'holes');

end
```

55

LEVEL SET ALGORITHM

function Contour_Image = Level_Set_Segmentation(InputImage, InitialMask, Timestep, Alpha, Num_Iterations)

   ** Note: The following algorithm is referred from a code written by Chunming Li.

% ------ Input Variables ------ %
% InputImage: Input Image
% Initial Mask: Initial contour, to be selected inside or outside the region that has to be
        segmented
% Timestep: Determines the speed of curve evolution.(Relatively large time steps can
              be used in the finite difference scheme to reduce the number of iterations
        and computational time, while ensuring sufficient numerical accuracy.)
% Alpha: A nonzero Alpha value gives additional extra force to drive the motion of
        the contour. (For weaker boundaries in the image a lower value of alpha is
        recommended.)
% Num_Iterations : Number of iterations performed to update the Level Set Function.

% Computes the gradient of the smoothed image in X and Y direction.
   [X_Gradient, Y_Gradient] = gradient(InputImage);
temp = X_Gradient.^2 + Y_Gradient.^2;   % Computes magnitude of the gradient.
Edge_Idicator_Function = 1 ./(1 + temp);

Initial_LevelSet_Function = -2*(InitialMask);
Initial_LevelSet_Function(Initial_LevelSet_Function == 0) = 2;
Contour_Image = Initial_LevelSet_Function;

   Epsilon   = 1.5;
   Lambda   = 5;
Myu   = 0.2 / Timestep;

% It computes the X and Y gradient of Edge indicator function.
   [gx, gy] = gradient(Edge_Idicator_Function);

for n = 1:Num_Iterations

    [ContourImage_Xgradient,ContourImage_Ygradient] = gradient(Contour_Image);
    % phi = Contour_Image
    s=sqrt(ContourImage_Xgradient.^2 + ContourImage_Ygradient.^2);
    % magnitude(grad(phi))

% It evaluates [grad(phi) / magnitude(grad(phi))]
Nx=ContourImage_Xgradient./(s+1e-10);
Ny=ContourImage_Ygradient./(s+1e-10);

56

```matlab
    % computes divergence
    [in1_Xgradient, ~] = gradient(Nx);
    [~, in1_Ygradient] = gradient(Ny);
    Curvature = in1_Xgradient + in1_Ygradient;

    [ContourImage_Xgradient, ContourImage_Ygradient] = gradient(Contour_Image);
    temp1 = sqrt(ContourImage_Xgradient.^2 + ContourImage_Ygradient.^2);
    temp2 = (temp1>=0) & (temp1<=1);
    temp3 = (temp1>1);

    Double_Well_Potential_FOD= ...
temp2 .* ( sin(2*pi*temp1) / (2*pi) ) + temp3 .* (temp1-1) ;
    Double_Well_Potential_FOD(Double_Well_Potential_FOD==0) = 1;
    temp1(temp1 == 0) = 1;
    DPS = Double_Well_Potential_FOD ./ temp1;


    Temp1 = DPS .* ContourImage_Xgradient - ContourImage_Xgradient;
    Temp2 = DPS .* ContourImage_Ygradient - ContourImage_Ygradient;
    % computes divergence
    [in1_Xgradient1, ~] = gradient(Temp1);
    [~, in1_Ygradient2] = gradient(Temp2);
    Temp3 = in1_Xgradient1 + in1_Ygradient2;


    % Evaluates Distance Regularization term.
    Distance_Regulization_Term = Temp3 + 4 * del2(Contour_Image);

    temp11 = (1/(2*Epsilon)) * ( 1 + cos(pi * Contour_Image/Epsilon) );
    temp21 = (Contour_Image<= Epsilon) & (Contour_Image>= -Epsilon);
    Dirac_Contour_Image = temp11 .* temp21;

    Area_Term = Dirac_Contour_Image .* Edge_Idicator_Function;
    Edge_Term = Dirac_Contour_Image .* (gx.*Nx + gy.*Ny) + ...
        Dirac_Contour_Image .* Edge_Idicator_Function .* Curvature ;

    Contour_Image = Contour_Image + Timestep * (           ...
                            Myu* Distance_Regulization_Term+ ...
                                Lambda* Edge_Term +               ...
                              Alpha * Area_Term );
    end

    % At the end of for loop, the Contour_Image variable holds the updated mask for the
    image.
```

B-SPLINE IMAGE REGISTRATION ALGORITHM

```matlab
[x1,y1,x2,y2] = InitialSeeds(Input_Image, Reference_Image, n);

%  Input Variables description
%Input_Image : It is the input image which has to be registered according to the
        reference image.
    %Reference_Image : It is the reference image.
    % n: It is the distance between the landmarks (pixels) on the circumference of the i
        input image. (n can any value above 1, best if it is set to a value between 2 and 5)

%  Output Variables description
    % x1, y1, and x2,y2 are the landmarks for the Input and Reference images
        respectively.


% Following functions "point_registration" and "bspline_transform" are written
    %by Dirk-Jan Kroon and it is available freely on web under the title "B-spline Grid,
    %Image and Point based Registration".

    [O_trans, Spacing]=point_registration(size(Input_Image),[x2(:) y2(:)],...
                                          [x1(:) y1(:)],3);

Ireg = bspline_transform(O_trans,Input_Image,Spacing,3);

    %  Displaying input, registered and reference images.
figure,
subplot(1,3,1),imshow(Input_Image, [0 max(Input_Image(:))]);
    title('Input Image');

subplot(1,3,2),imshow(Ireg, [0 max(Ireg(:))]);
    title('Registered Image');

    subplot(1,3,3),imshow(Reference_Image, [0 max(Reference_Image(:))]);
    title('Reference Image');
```

```matlab
function [x1,y1,x2,y2] = InitialSeeds(R1, R2, n)

    R1e = R1-double(bwmorph(R1, 'erode')); R2e = R2-double(bwmorph(R2, 'erode'));
ImSize = size(R1);

ColInit = ImSize(2);
while (1)
if max(R1e(:,ColInit))==0, ColInit = ColInit - 1;else ColNum = ColInit; break, end
end

RowInit = ImSize(1);
while (1)
if max(R1e(RowInit, ColInit))==0, RowInit = RowInit - 1;
else RowNum = RowInit; break, end
end
    R1_RowNum = RowNum;          R1_ColNum = ColNum;

ColInit = ImSize(2);
while(1)
if max(R2e(:,ColInit))==0, ColInit = ColInit - 1;else ColNum = ColInit; break, end
end

RowInit = ImSize(1);
while(1)
if max(R2e(RowInit, ColInit))==0, RowInit = RowInit - 1;
else RowNum = RowInit; break, end
end

    R2_RowNum = RowNum;          R2_ColNum = ColNum;
    contour1 = bwtraceboundary(R1e, [R1_RowNum, R1_ColNum], 'W', 8, ...
length(nonzeros(R1e)),'counterclockwise');
    contour2 = bwtraceboundary(R2e, [R2_RowNum, R2_ColNum], 'W', 8, ...
length(nonzeros(R2e)),'counterclockwise');

    Cout1 = contour1(1:n:end, :);
for i1 = 1:length(Cout1)
    i2 = round(i1*(length(contour2)/length(Cout1)));Cout2(i1,:) = contour2(i2,:);
end

Im1 = R1e; for n = 1:length(Cout1), Im1(Cout1(n,1), Cout1(n,2)) = 4;end
Im2 = R2e;for n = 1:length(Cout2), Im2(Cout2(n,1), Cout2(n,2)) = 4;end

    x1 = Cout1(:,1);   y1 = Cout1(:,2);   x2 = Cout2(:,1);   y2 = Cout2(:,2);

end
```